

Residual stress analysis of aluminum nitride piezoelectric micromachined ultrasonic transducers using Raman spectroscopy

James Spencer Lundh¹, Kathleen Coleman², Yiwen Song¹, Benjamin A. Griffin³, Giovanni Esteves⁴, Erica A. Douglas⁴, Adam Edstrand⁴, Stefan C. Badescu⁵, Elizabeth A. Moore⁵, Jacob H. Leach⁶, Baxter Moody⁷, Susan Trolier-McKinstry², and Sukwon Choi^{1,a)}

¹ *Department of Mechanical Engineering, The Pennsylvania State University, University Park, PA, 16802, USA*

² *Department of Materials Science and Engineering, The Pennsylvania State University, University Park, PA, 16802, USA*

³ *Defense Advanced Research Projects Agency, Arlington, VA 22203, USA*

⁴ *Sandia National Laboratories, Albuquerque, NM, 87185, USA*

⁵ *Air Force Research Laboratory, Wright-Patterson Air Force Base, OH, 45433, USA*

⁶ *Kyma Technologies, Inc., Raleigh, NC, 27617, USA*

⁷ *HexaTech, Inc., Morrisville, NC, 27560, USA*

Abstract

In this study, the Raman biaxial stress coefficients K^{II} and strain-free phonon frequencies ω_0 have been determined for the E_2 (low), E_2 (high), and A_1 (LO) phonon modes of aluminum nitride, AlN, using both experimental and theoretical approaches. The E_2 (high) mode of AlN is recommended for the residual stress analysis of AlN due to its high sensitivity and the largest signal-to-noise ratio amongst the studied modes. The E_2 (high) Raman biaxial stress coefficient of $-3.8 \text{ cm}^{-1}/\text{GPa}$ and strain-free phonon frequency of 656.68 cm^{-1} were then applied to perform both macroscopic and microscopic stress mapping. For macroscopic stress evaluation, the spatial variation of residual stress was measured across an AlN-on-Si wafer prepared by sputter deposition. A cross-wafer variation in residual stress of $\sim 150 \text{ MPa}$ was observed regardless of the average stress state of the film. Microscopic stress evaluation was performed on AlN piezoelectric micromachined ultrasonic transducers (pMUTs) with submicron spatial resolution. These measurements were used to assess the effect of device fabrication on the residual stress distribution in an individual pMUT and the effect of residual stress on the resonance frequency. In the $\sim 20 \text{ }\mu\text{m}$ directly outside the outer edge of the pMUT electrode, a large lateral spatial variation in residual stress of $\sim 100 \text{ MPa}$ was measured, highlighting the impact of metallization structures on residual stress in the AlN film.

Keywords: aluminum nitride (AlN), microelectromechanical systems (MEMS), residual stress, Raman spectroscopy, biaxial stress coefficient, strain-free phonon frequency, piezoelectric micromachined ultrasonic transducer (pMUT), resonance frequency

^{a)} Author to whom correspondence should be addressed: sukwon.choi@psu.edu

1. Introduction

Aluminum nitride (AlN) is important in numerous applications due to its piezoelectric nature, direct wide bandgap (~6.2 eV), high thermal conductivity (~285 W/mK), low thermal expansion coefficient, high elastic modulus, and high acoustic velocity^{1,2}. Research has demonstrated that AlN can be used to fabricate deep ultra-violet light emitting diodes (LEDs)³, high electron mobility transistor (HEMT) structures^{4,5}, and piezoelectric resonators^{6,7}. The introduction of AlN-based film bulk acoustic resonators (FBARs)^{6,7} into duplexer technology has allowed the telecommunication industry to provide an enhanced filter solution. In addition to the FBAR, various other microelectromechanical system (MEMS) devices have been fabricated that provide unique capabilities: piezoelectric micromachined ultrasonic transducers (pMUTs)⁸⁻¹⁰, surface acoustic wave (SAW) devices¹¹, contour mode resonators (CMRs)¹², flexural plate wave (FPW) devices¹³, and energy harvesting devices¹⁴. These structures have various far-reaching applications such as wireless communications^{6,7,10,15}, energy harvesting^{14,16}, medical imaging^{8,10}, ranging/proximity detection^{8,10}, microphones^{7,17}, strain sensors⁷, temperature sensors¹¹, biosensors¹⁸, chemical sensors⁷, accelerometers^{7,19}, biometric security^{9,10}, flexible and wearable electronics^{10,16}, and implantable biomedical devices^{10,16}.

However, the growth of AlN on non-native substrates results in residual stress which affects manufacturability, performance, and reliability. Residual stress can degrade piezoelectricity^{10,20}, alter resonance frequency^{8,19}, and affect acoustic phase velocity^{13,15}. Excessive residual stress can also lead to significant curvature in free-standing structures¹⁵ and damage, delamination, buckling, or cracking of films, ultimately restricting component lifetime^{13,21}. Therefore, the control and quantification of residual stress in AlN thin films is crucial to enable continued advancement and optimization of AlN-based MEMS and electronics.

Residual stress in AlN thin films is typically quantified through the wafer bow or wafer curvature method^{13,15,20,22-32} using the Stoney equation³³. The major limitation of the wafer curvature method is that it is a macroscopic stress evaluation technique that provides an average stress for the entire film. Other techniques that have been used to measure residual stress in AlN thin films include the ion beam layer removal (ILR) method³⁴, bulge testing³⁵, X-ray diffraction (XRD)^{2,29,36,37}, Fourier transform infrared spectroscopy (FTIR)^{29,38,39}, and Raman spectroscopy^{13,40-45}. The former two methods both require fabrication of test structures (and hence are destructive) and they have spatial resolutions on the order of hundreds of micrometers. Lab source XRD does not require any additional fabrication for stress evaluation but also suffers from spatial resolutions that are typically on the order of hundreds of micrometers⁴⁶. FTIR has a significantly improved spatial resolution of approximately 5-10 μm , but Raman spectroscopy can achieve submicron spatial resolution due to the use of visible radiation as opposed to infrared radiation⁴⁷. Raman spectroscopy can be applied to non-destructively measure stress distributions of entire wafers for process monitoring and control⁴⁸ or stress distributions of individual MEMS structures^{13,41} with submicron spatial resolution.

The residual stress in the film is determined experimentally with Raman spectroscopy by measuring the frequency, ω , of an individual phonon mode with respect to its strain-free frequency, ω_0 , at room temperature. The relationship between the phonon frequency shift, $\Delta\omega$, and residual stress in the film, σ_{film} , is described by⁴⁹:

$$\omega - \omega_0 = \Delta\omega = K^I \sigma_{film} \quad (1)$$

Table I. Previously reported values of the strain-free frequencies ω_0 and biaxial stress coefficients K^{II} for the E₂ (low), E₂ (high), and A₁ (LO) phonon modes of wurtzite aluminum nitride.

Ref.	E ₂ (low) ω_0 [cm ⁻¹]	E ₂ (high) ω_0 [cm ⁻¹]	A ₁ (LO) ω_0 [cm ⁻¹]	E ₂ (low) K^{II} [cm ⁻¹ /GPa]	E ₂ (high) K^{II} [cm ⁻¹ /GPa]	A ₁ (LO) K^{II} [cm ⁻¹ /GPa]
1	252	660	893			
13					-4.7 ± 0.5	
15		654			-3.5 ± 0.5	
27		658			-3.7 ± 0.3	
50	246.1 ± 0.5	655.1 ± 0.5	888.9 ± 0.5			
51					-3 ± 0.4	
52	247.5 ± 0.5	655.5 ± 0.1	891			
53					-2.55	
54		657.1			-4.45	
55		657.6			-4.1 ± 0.3	
56				0.94	-2.56	-2.22
57					-3.39 ± 0.64	-1.39 ± 0.28
58	248.6 ± 0.2	657.4 ± 0.2	890 ± 0.2			
59	247.3	656.52		0.713	-4.423	
60	241	667	898	0.94	-2.55	-2.21
61		657.67			-4.04 ± 0.3	
62					-3.4 ± 0.22	-3.12 ± 0.58
63		656			-2.9 ± 0.3	
64		657.8 ± 0.3			-2.4 ± 0.2	
65					-1.9	
66	247.8	656.5	888.4			
67		657.4 ± 0.2			-6.3 ± 1.4	

where K^{II} is the biaxial stress coefficient⁶⁸. Equation (1) assumes a state of biaxial stress, a typical assumption for thin films^{69,70}. For wurtzite AlN, three phonon modes that can be probed using Raman spectroscopy in the $Z(XX)\bar{Z}$ geometry are the E₂ (low), E₂ (high), and A₁ (LO) phonons⁴⁸. In Figure 1, these phonons are highlighted in the Raman spectra of free-standing bulk AlN, an AlN film on sapphire, and an AlN film on Si. Table I presents a compilation of previously reported K^{II} and ω_0 values for the E₂ (low), E₂ (high), and A₁ (LO) phonon modes of wurtzite AlN. As can be seen, reports of K^{II} and ω_0 for the E₂ (low) and A₁ (LO) modes in the literature are lacking. Additionally, while there are many values reported for K^{II} and ω_0 of the E₂ (high) mode, the range of these reported values is quite large.

In this study, the biaxial stress coefficient, K^{II} , and the strain-free phonon frequency, ω_0 , for the E₂ (low), E₂ (high), and A₁ (LO) phonon modes of wurtzite AlN are determined using Raman spectroscopy, COMSOL Multiphysics, and density functional theory (DFT) simulation. Subsequently, K^{II} and ω_0 of the E₂ (high) mode are applied to study residual stress distributions at both the macroscopic and microscopic levels through wafer-level and device-level measurements, respectively.

2. Methods

To determine the strain-free phonon frequencies (ω_0), a 1 in. free-standing bulk AlN wafer was prepared via a combination of seeded growth and physical vapor transport (PVT). Assuming that the free-standing bulk sample represents the strain-free aluminum nitride crystal, probing the AlN wafer with Raman spectroscopy yields the strain-free phonon frequencies of the E₂ (low), E₂ (high), and A₁ (LO) phonons of AlN.

To determine the Raman biaxial stress coefficients for the E_2 (low), E_2 (high), and A_1 (LO) modes of AlN, two methods were used. These methods were (1) a thermomechanical analysis approach using both Raman spectroscopy and COMSOL Multiphysics and (2) DFT modeling. The theory and application of these methods will be discussed in more detail in the following subsections.

2.1 Thermomechanical analysis

The thermomechanical analysis approach utilizes temperature-induced thermoelastic stresses to determine the biaxial stress coefficients. For free-standing bulk AlN, it is assumed that isothermal heating results in stress-free thermal expansion. Therefore, the frequency shift $\Delta\omega_{bulk}$ of the E_2 (low), E_2 (high), and A_1 (LO) phonons in free-standing bulk AlN should be solely due to temperature-induced effects.

For an AlN thin film on a substrate, thermoelastic stresses are induced by isothermal heating of the heterostructure due to the mismatch in the coefficients of thermal expansion between the AlN film and the substrate. These thermoelastic stresses introduce an additional contribution $\Delta\omega_S$ to the frequency shift $\Delta\omega_{film}$ of the phonons in the thin film AlN. Accordingly, the temperature dependence of the phonon frequency shifts in free-standing bulk AlN and thin film AlN will be different. This difference should be a result of thermally-induced biaxial stresses in the film.

In Figure 2, the difference between the frequency shift of the E_2 (high) phonon mode for free-standing bulk AlN and a 400 nm AlN thin film is shown. As can be seen, this difference $\Delta\omega_S$ follows an approximately linear relationship which is related to the E_2 (high) biaxial stress coefficient $K_{E_2}^{II} (high)$ and thermoelastic biaxial stress $\Delta\sigma$ by:

$$\Delta\omega_S = \Delta\omega_{film} - \Delta\omega_{bulk} = K_{E_2}^{II} (high) \Delta\sigma \quad (2)$$

The temperature dependence of the thermoelastic biaxial stress induced in the thin film can be computed by varying the environmental temperature in a thermomechanical model of the heterostructure using COMSOL Multiphysics. Therefore, the biaxial stress coefficients for the phonon modes of AlN can be determined using this modeled stress and the measured frequency shifts.

In this study, Raman spectroscopy was used to measure the frequencies of the E_2 (low), E_2 (high), and A_1 (LO) phonons of three AlN thin films (Table II, Samples 1-3) and a free-standing bulk AlN sample (Table II, Sample 4). The plasma vapor deposition with nanocolumns (PVDNC) film (Table II, Sample 1) was grown using Kyma's modified AlN sputtering technique to produce nanocolumnar arrays of AlN structures. Samples 2 and 3 of Table II were purchased from a commercial vendor (Nitride Solutions) and were grown via hydride vapor phase epitaxy (HVPE) and PVT using a proprietary process for producing high-quality nitride templates with high ultraviolet (UV) transparency and low defectivity. The free-standing bulk AlN substrate (Table II, Sample 4) was produced by HexaTech using their proprietary crystal growth process. This process creates high quality single crystalline AlN boules for the fabrication of AlN substrates (Table II, Sample 4). The AlN substrates provided by HexaTech have an average dislocation density of 10^2 - 10^4 cm^{-2} .

For temperature dependent measurements, all samples were placed in a temperature controlled Linkam stage for isothermal heating. For all measurements in this study, Raman spectroscopy was performed with a Horiba LabRAM HR Evolution spectrometer using a 532 nm laser and an 1800 grooves/mm grating. Measurements were performed in a 180° backscattering configuration, i.e., $Z(XX)\bar{Z}$ geometry. For Raman temperature calibrations, a 50X super long working distance objective (NA = 0.45) was used, offering a spatial resolution of ~ 1 μm . This was due to limitations on the objective working distance imposed by the

Linkam thermal stage. For all other measurements, a 100X long working distance objective (NA = 0.8) was used, offering a spatial resolution of $< 1 \mu\text{m}$. The system was calibrated using the single crystal Si peak at 520.7 cm^{-1} and the E_2 (TO) phonon mode of single crystal 4H-SiC at 776.839 cm^{-1} . A mercury emission line at $\sim 546 \text{ nm}$ ($\sim 480 \text{ cm}^{-1}$) was used as a reference in order to monitor and correct for systematic spectral drift from error sources such as room temperature fluctuations. For measurement of AlN films on sapphire, a laser power of 15 mW was used since both AlN and sapphire are optically transparent to the sub-bandgap laser energy ($\sim 2.33 \text{ eV}$). For measurements of AlN on Si, the laser power was reduced to $\sim 1 \text{ mW}$ in order to prevent laser heating of the Si substrate. For temperature dependent measurements, the measurement acquisition time was monitored and, if needed, increased such that a relatively constant Raman peak intensity (within ± 2000 counts) was maintained throughout the experiment.

Table II. Details of the 4 AlN samples used in the thermomechanical analysis approach.

Sample Number	Substrate	AlN thickness [nm]	Deposition/Growth Method
1	Sapphire	400	PVDNC*
2	Sapphire	481	PVT
3	Sapphire	1007	HVPE
4	AlN (free-standing bulk)	6×10^5 (free-standing bulk)	Seeded/PVT

*Plasma vapor deposition with nanocolumns (see Supplementary Material)

COMSOL Multiphysics was used to build a 3D finite element thermomechanical model of the AlN/sapphire heterostructure for Samples 1-3 using the temperature dependent coefficients of thermal expansion for AlN⁷¹ and sapphire⁷² listed in Supplementary Table I and the stiffness coefficients of AlN⁷³ and sapphire⁷⁴. Stiffness coefficients can be experimentally determined based on bulk or thin film materials. Thin films often grow with a columnar microstructure and the column boundaries may be lower density, which could act to lower the stiffness coefficients.^{75,76} Since the thermomechanical model and approach are based on thin film AlN, stiffness coefficients experimentally determined based on thin film AlN⁷³ were used in the model. Thermoelastic stresses induced in the AlN film at the elevated temperature conditions were the modeled outputs. As Raman spectroscopy measures through the entire thickness of the AlN film, a volumetric element similar to the Raman probing volume was used to obtain the through-thickness average stress values from the simulation.

2.4 Density functional theory modeling

Experimentally, the residual stress in the thin film is determined by the frequency shift, $\Delta\omega$, of the measured phonon frequency, ω , with respect to the strain-free phonon frequency, ω_0 , as shown in Equation (1). Ultimately, the residual stress characterization of AlN via Raman spectroscopy can be explained by linear phonon deformation potential theory. Phonon deformation potential theory describes the change in the interatomic potential of the crystal due to small perturbations arising from strain. This change in the interatomic potential results in a shift of the phonon frequency. Through simplifying assumptions, including biaxial residual stress, it can be shown that the strain phonon deformation potentials (PDPs) can be used to calculate the biaxial stress coefficient K^{II} (see Supplementary Material).

Density functional theory (DFT) is a computational modeling method that can determine the strain PDPs. For the first principles calculations, the method used was previously verified for wurtzite GaN⁷⁷. This method used the Perdew-Zunger local density approximation (PZ-LDA) of DFT implemented in the QUANTUM ESPRESSO code⁷⁸, projector-augmented wave (PAW) pseudopotentials with plane-wave

cutoffs of 60 Ry and 240 Ry for the energy and electronic density, respectively, and a $12 \times 12 \times 8$ Brillouin zone sampling grid. The phonon spectra were calculated using a single unit cell within the density functional perturbation theory (DFPT) formalism⁷⁹. This choice of density functional and pseudopotentials was found to be consistent with experimental values of the lattice parameters, elastic constants, and phonon frequencies. The strain PDPs entering into the biaxial stress coefficients were calculated from seven equally spaced strain values from -0.005 to 0.005. For the electric field coefficients, the QUANTUM ESPRESSO implementation of the modern theory of polarization was used⁸⁰, taking seven equally spaced electric field values in the range from -9 MV/cm to 9 MV/cm. Using the elastic constants of AlN and the strain PDPs determined through DFT simulations, the biaxial stress coefficients for the E_2 (low), E_2 (high), and A_1 (LO) phonon modes can be determined (see Supplementary Material).

Table III. Summary of the biaxial stress coefficients of the E_2 (low), E_2 (high), and A_1 (LO) phonon modes of wurtzite AlN determined in this study. The two submethods listed in “DFT” are two adaptations of the DFT modeling approach.

Method	Submethod	E_2 (low) K'' [cm ⁻¹ /GPa]	E_2 (high) K'' [cm ⁻¹ /GPa]	A_1 (LO) K'' [cm ⁻¹ /GPa]
Thermomechanical analysis	N/A	1.10 ± 0.02	-3.80 ± 0.04	-2.68 ± 0.04
	PBESol	0.77	-3.46	-2.08
DFT	PZ	0.82	-3.46	-2.36

3. Results and Discussion

3.1 Determination of the biaxial stress coefficients and strain-free phonon frequencies

The strain-free phonon frequencies of the E_2 (low), E_2 (high), and A_1 (LO) phonons of AlN were determined by probing the free-standing bulk AlN substrate (Table II, Sample 4) using Raman spectroscopy. To account for possible spatial variations, measurements were performed in 1 mm increments from the center towards the edge of the 1 in. (25.4 mm) wafer. At each location, 50 measurements were performed, resulting in a total of 550 measurements on the free-standing bulk AlN substrate. From this study, the E_2 (low), E_2 (high), and A_1 (LO) modes of the free-standing bulk AlN substrate were measured to be 247.84 ± 0.004 , 656.68 ± 0.003 , and 888.97 ± 0.005 cm⁻¹.

These phonon frequencies are very similar to those reported in Ref.⁶⁶ (see Table I) where an extensive Raman study was performed on bulk AlN crystals. Moreover, using X-ray diffraction (XRD), the lattice parameters of the free-standing bulk AlN substrate were determined to be $a = 3.11$ Å and $c = 4.979$ Å which shows agreement within 0.1% of previous reports for the lattice parameters of AlN^{81–84}. Therefore, the phonon frequencies measured for the free-standing bulk AlN substrate are assumed to represent the strain-free phonon frequencies of the E_2 (low), E_2 (high), and A_1 (LO) phonons of AlN for this study.

The biaxial stress coefficients of the E_2 (low), E_2 (high), and A_1 (LO) phonons of AlN were determined using two methods. As discussed in Section 2.1, the first method, thermomechanical analysis, depends on comparing the temperature dependence of measured phonon frequencies in a bulk and thin film sample. Since the thin film will experience thermoelastic stress due to a mismatch in the coefficient of thermal

expansion with the substrate, it is possible to separate the effect of in-plane biaxial stress from temperature on phonon frequency. In order to determine these thermoelastic stresses, a 3D thermomechanical model of the three AlN/sapphire heterostructures (Table II, Samples 1-3) was constructed. The modeled stresses in the c-plane (σ_{xx} , σ_{yy}) are approximately identical while the shear stress (σ_{xy}) and out-of-plane stress (σ_{zz}) are negligible, validating the assumption of biaxial stress in the c-plane in the model (see Supplementary Figure 2). Analytical calculations were also performed to determine the film stress which showed close agreement with the film stress determined via COMSOL Multiphysics (see Supplementary Figure 3).

The effect of biaxial stress on the frequency shift was determined by the difference between the temperature dependence of the measured phonon frequency shifts of the three AlN films (Table II, Samples 1-3) and the free-standing bulk AlN substrate (Table II, Sample 4) according to Equation (2). The modeled temperature dependent biaxial stresses $\Delta\sigma$ in the three thin films were then related to the stress-induced frequency shifts as shown in Figure 3. Linear fitting of the data in Figure 3 was used to determine the biaxial stress coefficient for each phonon mode (the slope of the fit as shown in Equation (2)). From Figure 3, the direction of frequency shift with stress and relative sensitivity to stress of the various phonon modes observed using this method are similar to those reported in Table I. The E_2 (low) and E_2 (high) phonon modes show consistency amongst all three films; however, for the A_1 (LO) phonon mode, only Samples 1 and 2 show good agreement.

While the E_2 modes are non-polar and only affected by temperature and stress, the A_1 modes are polar and phonon-plasmon coupled modes. An increase in free electron concentration can significantly increase both the frequency and linewidth of the A_1 (LO) mode. For example, studies on n-type GaN have shown an increase of the A_1 (LO) frequency from 738 cm^{-1} to 743 cm^{-1} for an increase in free carrier concentration from $n = 1.2 \times 10^{17} \text{ cm}^{-3}$ to $2.2 \times 10^{17} \text{ cm}^{-3}$.⁴⁸ Additionally, it has been shown that the linewidth of the A_1 (LO) mode increased from 6.7 cm^{-1} for unintentionally doped GaN to $\sim 70 \text{ cm}^{-1}$ for n-doped GaN with a carrier concentration of $n = 2.5 \times 10^{18} \text{ cm}^{-3}$.⁸⁵

The linewidth of the A_1 (LO) mode in Samples 1 and 2 is $\sim 9 \text{ cm}^{-1}$ while in Sample 3 it is approximately 12 cm^{-1} . This increased linewidth in Sample 3 could be due to lower crystal quality, increased free carrier concentration, or a combination of both. Additionally, as the temperature was increased during the Raman temperature calibration of Sample 3, it is possible that the combination of the laser energy and increased thermal energy allowed finite activation of electrons. This would locally increase the free carrier concentration in Sample 3 and cause the A_1 (LO) phonon frequency to increase without affecting the E_2 (low) and E_2 (high) phonon frequencies. This would reduce the magnitude of $\Delta\omega$ in Figure 3(c). Therefore, it is hypothesized that this discrepancy could be due to phonon-plasmon coupling of the A_1 (LO) mode, and the biaxial stress coefficient derived from Sample 3 for the A_1 (LO) was disregarded for averaging purposes.

Finally, DFT modeling was used to determine the phonon deformation potentials of the E_2 (low), E_2 (high), and A_1 (LO) phonon modes. Two separate approaches were used: the PBESol functional and LDA-PZ. The phonon deformation potentials determined using DFT were used to calculate biaxial stress coefficients for all phonon modes.

A summary of the biaxial stress coefficients for the E_2 (low), E_2 (high), and A_1 (LO) phonon modes of AlN determined by the thermomechanical approach and DFT modeling is shown in Table III. Three different biaxial stress coefficients are reported for each phonon of interest. In general, there is good agreement between the biaxial stress coefficients determined via the thermomechanical analysis and DFT modeling. Therefore, the results of the thermomechanical analysis method were adopted.

3.2 Validation of the biaxial stress coefficients and strain-free phonon frequencies

After determining the biaxial stress coefficients and strain-free phonon frequencies, a validation study

was performed (see Supplementary Material). This was accomplished by measuring the frequencies of the E_2 (low), E_2 (high), and A_1 (LO) phonons of several AlN thin films using Raman spectroscopy. Subsequently, ω_0 and K'' determined in Section 3.1 were applied to compare the residual stress calculated using all three phonon modes in the various films (see Supplementary Figure 4). For all samples, there was relatively good agreement in the nature (tensile vs. compressive) and magnitude of the residual stress.

Additionally, XRD was performed to determine the strain in the a-direction (ϵ_a) and c-direction (ϵ_c) for all films (see Supplementary Material for methodology) and then to calculate the strain ratio ϵ_c/ϵ_a . The strain ratios for the films were then compared to the theoretical strain ratio of -0.608 for biaxial strain in wurtzite AlN⁸⁶ (see Supplementary Figure 4). For the samples used in the validation study, the closest strain ratio to the theoretical value of -0.608 was -0.71. For this film (Supplementary Figure 4, Sample 1), the residual stresses calculated using all three phonon modes are -2.72 ± 0.067 , -2.74 ± 0.032 , and -2.66 ± 0.047 GPa, which agree within 3%.

When using Raman spectroscopy for residual stress analysis of AlN thin films and devices, it is recommended that the E_2 (high) phonon mode be used for several reasons. First, the E_2 (high) phonon mode demonstrates the greatest sensitivity to stress. Second, the E_2 (high) Raman peak has the greatest intensity, resulting in the shortest acquisition time for Raman measurements and the largest signal-to-noise ratio (Figure 1). Finally, in contrast to the phonon-plasmon coupled A_1 (LO) phonon mode, the frequency of the E_2 (high) mode is not affected by the free carrier concentration; therefore, only stress will affect this phonon frequency for residual stress measurements.

To demonstrate the advantages of using Raman spectroscopy for residual stress characterization, both wafer-level (Section 3.3) and device-level (Section 3.4) stress characterization were performed. Wafer-level stress characterization involved measuring the residual stress distribution across wafers with different average stress states determined via the wafer curvature method. Device-level characterization was performed on AlN pMUTs. Residual stress mapping was performed on an individual pMUT from the center of the released diaphragm to the clamped region. In addition, the effect of residual stress on resonant frequency in the pMUTs was studied.

Table IV. Recommended values of the strain-free phonon frequencies and biaxial stress coefficients for the E_2 (low), E_2 (high), and A_1 (LO) phonon modes of wurtzite AlN.

	ω_0 [cm ⁻¹]	K'' [cm ⁻¹ /GPa]
E_2 (low)	247.84 ± 0.004	1.10 ± 0.02
E_2 (high)	656.68 ± 0.003	-3.80 ± 0.04
A_1 (LO)	888.97 ± 0.005	-2.68 ± 0.04

3.3 Wafer-level stress characterization

Raman spectroscopy was performed on an AlN-on-Si wafer (150 mm diameter) to investigate the residual stress distribution across the wafer at the macroscopic level. Raman stress measurements were conducted at 10 mm increments across 100 mm of the diameter of the wafer. Since the probing depth of the 532 nm laser (NA = 0.8) is $\geq 1 \mu\text{m}$ ⁸⁷ in materials whose bandgap is greater than the laser energy of ~ 2.33 eV, the entire through thickness of the AlN film (~ 750 nm) was probed. Therefore, a through-thickness average residual stress was measured.

As shown in Figure 4, the residual stress was found to become more compressive as the distance from the center of the wafer increased. Moreover, the Raman peak intensities of the E_2 (high) phonon decreased

with increasing distance from the center of the wafer. To determine whether this could be due to spatial non-uniformities in film thickness, spectroscopic ellipsometry was performed across the wafer. Film thickness measurements were performed using a J. A. Woollam M-2000XI Ellipsometer. Psi (Ψ) and delta (Δ) functions were collected versus wavelength (300 – 1000 nm) at angles of incidence of 50°, 60°, and 70°. All measurements were performed in room temperature air. From these measurements, a correlation was observed between the spatial variation in residual stress and the AlN film thickness as seen in Figure 4. Spatial variations in thickness are common in many sputter deposition systems⁸⁸. For these measurements, the local minima of film thickness observed in Figure 4 at ± 40 mm corresponds to the circular racetrack of the sputter deposition tool about 40 mm from the center of the sputter target.

The data of Figure 4 are in agreement with previous reports showing that the residual stress shifts towards more compressive stress as the thickness of sputter deposited AlN films decreases^{24,25}. This same correlation was found for three different AlN-on-Si wafers with varying stress states of tensile, compressive, and no average residual stress calculated via the wafer curvature method (see Supplementary Figure 5).

The results shown in Figure 4 highlight one advantage that Raman spectroscopy has for residual stress characterization over macro-scale approaches like the wafer curvature method: Raman spectroscopy can be used to resolve spatial non-uniformities in residual stress. This is important for device applications because residual stress⁸⁹ and thickness⁷ affect device performance leading to cross-wafer variability in device behavior. This also has important implications for next generation devices based on $\text{Al}_{1-x}\text{Sc}_x\text{N}$ since the residual stress can affect the piezoelectric properties and thus reduce performance for $\text{Al}_{1-x}\text{Sc}_x\text{N}$ devices⁹⁰⁻⁹².

3.4 Device-level stress characterization

Raman spectroscopy can also be used to analyze residual stress at the microscopic level. This is useful since materials processing and device fabrication affect the residual stress in as-prepared materials and devices. There have been many reports on the residual stress in AlN films resulting from varying the deposition parameters^{2,37,93-95}. With respect to devices, metallization can influence the residual stress following material processing. For instance, for AlGaN/GaN HEMTs, significant changes in the residual stress were reported near surface metallization structures⁴⁹. Furthermore, on AlN-based MEMS structures, buried electrode layers can influence the residual stress in the overlying AlN film⁴¹.

To demonstrate microscale residual stress analysis, Raman measurements were performed on AlN pMUTs. A cross-sectional schematic of the pMUT is shown in Figure 5(a). The devices in this study were made using a silicon-on-insulator (SOI) wafer. The AlN film was grown with the same processing used to grow Samples 5-13 in Supplementary Table II. The devices were released with a backside deep reactive-ion etch (DRIE) which lands on the buried oxide, and subsequently a wet etch with hydrofluoric (HF) acid was used to remove the oxide. The isotrench, made from low pressure chemical vapor deposition (LPCVD) polysilicon, helped prevent lateral etching when the wet etch was done.

In the first device-level study, the residual stress distribution as a function of distance across a pMUT was measured. A top-view schematic diagram of the pMUT and stress mapping is shown in Figure 5(b). The stress mapping is divided into regions A, B, and C. Region A consists of the released AlN pMUT diaphragm and extends from the center of the diaphragm to the inner edge of the top electrode of the pMUT (~ 420 μm). Measurements 1-20 were performed with 20 μm step sizes and the remaining measurements in region A were performed with 1 μm step sizes. Region B defines the immediate area outside of the top electrode (~ 20 μm). The measurements in region B were performed with 1 μm step

sizes. Finally, region C represents the region from ~ 20 - $2400 \mu\text{m}$ away from the outer edge of the top electrode ($50 \mu\text{m}$ step sizes). Both regions B and C consisted of the clamped AlN film.

Figure 5(c) displays the residual stress distribution as a function of measurement number. In region A, the residual stress distribution of the released diaphragm was uniform and there was no significant deviation in residual stress observed near the inner edge of the electrode. The average residual stress in region A was $\sim 475 \text{ MPa}$. In region B, the average residual stress is more tensile with a value of $\sim 560 \text{ MPa}$. However, there is a large residual stress variation directly outside the outer edge of the top electrode. Over a distance of $\sim 20 \mu\text{m}$, the residual stress decreases from a peak value of $\sim 610 \text{ MPa}$ down to roughly the average value of Region C ($\sim 510 \text{ MPa}$). In region C, the residual stress distribution is again observed to be uniform. However, when comparing the released AlN film of the pMUT diaphragm (region A) with the surrounding clamped AlN film (regions B and C), it can be seen that the clamped AlN film is more tensile. This was also observed in five identical pMUTs measured in the second study of this section. On average, all pMUTs were observed to have an average residual stress $\sim 35 \text{ MPa}$ more tensile outside the device structure (clamped AlN, region C) than in the pMUT diaphragm (released AlN, region A). This is reasonable considering relaxation of the AlN film (potentially by bending of the diaphragm) after release.

In the second study, the residual stress in different pMUTs were measured and compared with their resonant frequencies. It was hypothesized that variation in residual stress across the AlN/Si wafer on which the pMUTs were fabricated would show a correlation with the resonant frequencies of the pMUTs. To test this, the same device from identical reticles of a mask were measured at different locations on the wafer (see inset of Figure 6(a)). The frequency dependent response of the measured pMUTs are shown in the impedance plots of Figure 6(a). The residual stress as a function of resonant frequency is shown for the first, second, and third order modes in Figure 6(b).

Although the devices in reticles 4, 5, and 7 had a residual stress that agrees very well within the uncertainty in the measurement, the resonant frequencies for the first, second, and third order modes of these devices span a frequency range of ~ 13 , 13 , and 25 kHz . Furthermore, all devices show a resonant frequency within a range of $\sim 34 \text{ kHz}$ despite the large range of residual stresses measured ($\sim 110 \text{ MPa}$). This suggests that the diaphragm shape, diaphragm dimensions, boundary conditions, and electrode coverage dominated the change in frequency, rather than the residual stress^{9,96}. The devices in this study had an isotrench that was used to stop the HF etch from running laterally on the final device release, thus defining the radius of the device. During processing, this may have been compromised and an extension of the undercut from what was originally designed is possible. This would alter the resonant frequency of the designed device.

Furthermore, since the pMUTs were fabricated on wafers like those shown in Figure 4 and Supplementary Figure 5, they are expected to exhibit film thicknesses dependent on the radial distance from the center of the wafer. For these pMUTs, the radial distance from the center of the wafer for reticles 4-8 were approximately 4.3 , 4.2 , 6.2 , 4.1 , and 2.4 cm , respectively. Therefore, reticles 4, 5, and 7 were all approximately the same radial distance from the center of the wafer and should have close to the same film thickness. Based on the results of the wafer-level characterization shown in Figure 4 and Supplementary Figure 5, it is reasonable to assume that the devices in these reticles also possess similar levels of residual stress. This is indeed observed in the residual stress measurements of the devices in reticles 4, 5, and 7 as shown in Figure 6(b).

Reticle 6 is located the furthest from the center of the wafer (6.2 cm), where the film thickness was observed to increase (Figure 4). Therefore, one would expect the residual stress in the device in reticle 6 to be more tensile than in reticles 4, 5, and 7. This is observed in the data of Figure 6(b) where the residual

stress measured in the device in reticle 6 was seen to be ~ 30 MPa higher than those in reticles 4, 5, and 7. Finally, reticle 8 was the closest to the center of the wafer (2.4 cm) where the film thickness is appreciably greater than those of the devices in reticles 4-7. As expected, the device in reticle 8 had a residual stress ~ 80 MPa greater than that of reticle 6 and ~ 110 MPa greater than those of reticles 4, 5, and 7.

While the residual stress measured in the devices of reticles 4-8 (Figure 6) showed good qualitative agreement with respect to the radially dependent film thickness observed in Figure 4 and Supplementary Figure 5, the resonant frequencies of these devices did not show a clear trend with residual stress. Therefore, it is hypothesized that there are multiple contributing factors that are affecting the resonant frequency other than residual stress such as film thickness, processing, and diaphragm diameter, and these competing contributions convolute the dependency of resonant frequency on residual stress in this study.

4. Conclusions

In conclusion, the strain-free phonon frequencies ω_0 and Raman biaxial stress coefficients K^II for the E_2 (low), E_2 (high), and A_1 (LO) phonons of AlN have been determined and compared using two methods. These methods include (1) a thermomechanical analysis approach using Raman spectroscopy and COMSOL Multiphysics and (2) the DFT modeling approach. The K^II determined using the thermomechanical analysis approach and the ω_0 measured from the free-standing bulk AlN sample (Table IV) for the E_2 (high) phonon mode were applied to quantify the residual stress in AlN films on both macroscopic and microscopic scales by performing wafer-level and device-level characterization.

Wafer-level residual stress characterization with Raman spectroscopy showed a radial stress variation across AlN/Si wafers prepared by sputter deposition. Spectroscopic ellipsometry confirmed there was radial thickness variation in the film and showed a strong correlation with the measured residual stress. Device-level residual stress characterization was performed to monitor the effects of residual stress on resonant frequency. While the measured residual stress in various devices across the wafer were in good agreement with the results from wafer-level stress characterization, no clear trend was observed between resonant frequency and residual stress. This was hypothesized to be due to competing effects on resonant frequency from residual stress, film thickness, processing, and diaphragm diameter. The residual stress distribution of a pMUT device was also measured using submicron spatial resolution. The stress of the released AlN pMUT diaphragm was observed to be less tensile than the clamped AlN film outside of the device. Furthermore, a large lateral residual stress variation of ~ 100 MPa over a length of ~ 20 μm was observed directly outside the outer edge of the electrode.

In summary, Raman spectroscopy can be used to quantitatively assess the effect that many different deposition parameters and fabrication processes have on the residual stress in AlN films which is crucial for process monitoring and control. This capability is highly beneficial to enable efficient performance and design of AlN piezoMEMs device technologies.

Supplementary Material

See supplementary material for more detailed discussions on the relation between the phonon deformation potentials and biaxial stress coefficients, the thermomechanical analysis approach, the validation study, and the stress variation across wafers of different average residual stress states (tensile, no stress, compressive).

Acknowledgements

Funding for efforts by the Pennsylvania State University was provided by the Center for Dielectrics and Piezoelectrics and the National Science Foundation (Nos. IIP-1361571, IIP-1361503, IIP-1841453, and IIP-1841466) and the AFOSR Young Investigator Program (Grant No. FA9550-17-1-0141, Program Officers: Dr. Michael Kendra and Dr. Brett Pokines, also monitored by Dr. Kenneth Goretta). The authors would like to thank Joan M. Redwing (Pennsylvania State University) for assisting them with the structural characterization of the AlN thin films. Sandia National Laboratories is a multi-mission laboratory managed and operated by National Technology & Engineering Solutions of Sandia, LLC., a wholly owned subsidiary of Honeywell International, Inc., for the U.S. Department of Energy's National Nuclear Security Administration under contract DE-NA0003525. This paper describes objective technical results and analysis. Any subjective views or opinions that might be expressed in the paper do not necessarily represent the views of the U.S. Department of Energy or the United States Government.

Data Availability

The data that support the findings of this study are available from the corresponding author upon reasonable request.

References

- ¹ L.E. McNeil, M. Grimsditch, and R.H. French, *J. Am. Ceram. Soc.* **76**, 1132 (1993).
- ² H.Y. Liu, G.S. Tang, F. Zeng, and F. Pan, *J. Cryst. Growth* **363**, 80 (2013).
- ³ Y. Taniyasu, M. Kasu, and T. Makimoto, *Nature* **441**, 325 (2006).
- ⁴ A.G. Baca, A.M. Armstrong, A.A. Allerman, E.A. Douglas, C.A. Sanchez, M.P. King, M.E. Coltrin, T.R. Fortune, and R.J. Kaplar, *Appl. Phys. Lett.* **109**, 033509 (2016).
- ⁵ J. Cho, E. Bozorg-Grayeli, D.H. Altman, M. Asheghi, and K.E. Goodson, *IEEE Electron Device Lett.* **33**, 378 (2012).
- ⁶ R. Ruby, in *Proc. - IEEE Ultrason. Symp.* (2007), pp. 1029–1040.
- ⁷ G. Piazza, V. Felmetger, P. Muralt, R.H. Olsson, and R. Ruby, *MRS Bull.* **37**, 1051 (2012).
- ⁸ S. Shelton, M.L. Chan, H. Park, D. Horsley, B. Boser, I. Izyumin, R. Przybyla, T. Frey, M. Judy, K. Nunan, F. Sammoura, and K. Yang, in *Proc. - IEEE Ultrason. Symp.* (IEEE, 2009), pp. 402–405.
- ⁹ B.A. Griffin, A.M. Edstrand, S. Yen, and R.W. Reger, in *2018 IEEE Int. Ultrason. Symp.* (2018), pp. 1–4.
- ¹⁰ W. Kang, J. Ryu, W. Lee, J. Jung, E. Shin, and H. Choi, *J. Micromechanics Microengineering* **27**, 113001 (2017).
- ¹¹ C. Li, X. Liu, L. Shu, and Y. Li, *Mater. Express* **5**, 367 (2015).
- ¹² G. Piazza, P.J. Stephanou, and A.P. Al Pisano, *J. Micromechanical Syst.* **15**, 1406 (2006).
- ¹³ M. Reusch, K. Holc, W. Pletschen, L. Kirste, A. Žukauskaitė, T. Yoshikawa, D. Iankov, O. Ambacher, and V. Lebedev, *J. Vac. Sci. Technol. B, Nanotechnol. Microelectron. Mater. Process. Meas. Phenom.* **34**, 052001 (2016).
- ¹⁴ R. Elfrink, T.M. Kamel, M. Goedbloed, S. Matova, D. Hohlfeld, Y. Van Anandel, and R. Van Schaijk, *J. Micromechanics Microengineering* **19**, 094005 (2009).
- ¹⁵ M. Reusch, S. Cherneva, Y. Lu, A. Žukauskaitė, L. Kirste, K. Holc, M. Datcheva, D. Stoychev, V. Lebedev, and O. Ambacher, *Appl. Surf. Sci.* **407**, 307 (2017).
- ¹⁶ F. Guido, A. Quattieri, L. Algieri, E.D. Lemma, M. De Vittorio, and M.T. Todaro, *Microelectron. Eng.* **159**, 174 (2016).
- ¹⁷ M.D. Williams, B.A. Griffin, T.N. Reagan, J.R. Underbrink, and M. Sheplak, *J. Microelectromechanical Syst.* **21**, 270 (2012).
- ¹⁸ Y.Q. Fu, J.K. Luo, N.T. Nguyen, A.J. Walton, A.J. Flewitt, X.T. Zu, Y. Li, G. McHale, A. Matthews, E. Iborra, H. Du, and W.I. Milne, *Prog. Mater. Sci.* **89**, 31 (2017).
- ¹⁹ R.H. Olsson, K.E. Wojciechowski, M.S. Baker, M.R. Tuck, and J.G. Fleming, *J. Microelectromechanical Syst.* **18**, 671 (2009).
- ²⁰ E. Iborra, J. Olivares, M. Clement, L. Vergara, A. Sanz-Hervás, and J. Sangrador, *Sensors Actuators, A Phys.* **115**, 501 (2004).
- ²¹ R. Treml, D. Kozic, J. Zechner, X. Maeder, B. Sartory, H.P. Gänser, R. Schönggrundner, J. Michler, R. Brunner, and D. Kiener, *Acta Mater.* **103**, 616 (2016).
- ²² I. Gablech, V. Svatoš, O. Caha, A. Dubroka, J. Pekárek, J. Klempa, P. Neužil, M. Schneider, and T. Šikola, *Thin Solid Films* **670**, 105 (2019).
- ²³ A. Ababneh, U. Schmid, J. Hernando, J.L. Sánchez-Rojas, and H. Seidel, *Mater. Sci. Eng. B Solid-State Mater. Adv. Technol.* **172**, 253 (2010).
- ²⁴ F. Martin, P. Muralt, M.-A. Dubois, and A. Pezous, *J. Vac. Sci. Technol. A Vacuum, Surfaces, Film.* **22**, 361 (2004).
- ²⁵ P. Pobedinskas, J.C. Bolsée, W. Dexters, B. Ruttens, V. Mortet, J. D’Haen, J. V. Manca, and K. Haenen, *Thin Solid Films* **522**, 180 (2012).
- ²⁶ B.A. Griffin, M.D. Williams, C.S. Coffman, and M. Sheplak, *J. Microelectromechanical Syst.* **20**, 476 (2011).

- ²⁷ V. Lughi and D.R. Clarke, *Appl. Phys. Lett.* **89**, 1 (2006).
- ²⁸ B.K. Gan, M.M.M. Bilek, D.R. McKenzie, M.B. Taylor, and D.G. McCulloh, *J. Appl. Phys.* **95**, 2130 (2004).
- ²⁹ A. Pandey, S. Dutta, R. Prakash, R. Raman, A.K. Kapoor, and D. Kaur, *J. Electron. Mater.* **47**, 1405 (2018).
- ³⁰ G.F. Iriarte, F. Engelmark, M. Ottosson, and I.V. Katardjiev, *J. Mater. Res.* **18**, 423 (2003).
- ³¹ A.M. Engwall, Z. Rao, and E. Chason, *Mater. Des.* **110**, 616 (2016).
- ³² V.M. Mastronardi, F. Guido, M. Amato, M. De Vittorio, and S. Petroni, *Microelectron. Eng.* **121**, 59 (2014).
- ³³ G.G. Stoney, *Proc. R. Soc. London . Ser. A* **172** (1909).
- ³⁴ R. Schöngrundner, R. Treml, T. Antretter, D. Kozic, W. Ecker, D. Kiener, and R. Brunner, *Thin Solid Films* **564**, 321 (2014).
- ³⁵ E. Österlund, J. Kinnunen, V. Rontu, A. Torkkeli, and M. Paulasto-Kröckel, *J. Alloys Compd.* **772**, 306 (2019).
- ³⁶ J.T. Luo, B. Fan, F. Zeng, and F. Pan, *J. Phys. D: Appl. Phys.* **42**, 235406 (2009).
- ³⁷ P. Panda, R. Ramaseshan, N. Ravi, G. Mangamma, F. Jose, S. Dash, K. Suzuki, and H. Suematsu, *Mater. Chem. Phys.* **200**, 78 (2017).
- ³⁸ J.H. Edgar, C.A. Carosella, C.R. Eddy, and D.T. Smith, *J. Mater. Sci. Mater. Electron.* **7**, 247 (1996).
- ³⁹ H. Windischmann, *Thin Solid Films* **154**, 159 (1987).
- ⁴⁰ A. Severino and F. Iucolano, *Phys. Status Solidi Basic Res.* **253**, 801 (2016).
- ⁴¹ S. Choi and B.A. Griffin, *J. Micromechanics Microengineering* **26**, 025009 (2016).
- ⁴² J. Gleize, F. Demangeot, J. Frandon, M.A. Renucci, M. Kuball, F. Semond, and J. Massies, *Phys. Status Solidi Appl. Res.* **188**, 511 (2001).
- ⁴³ R.G. Banal, M. Imura, D. Tsuya, H. Iwai, and Y. Koide, *Phys. Status Solidi Appl. Mater. Sci.* **214**, 1600727 (2017).
- ⁴⁴ L. Liu, B. Liu, J.H. Edgar, S. Rajasingam, and M. Kuball, *J. Appl. Phys.* **92**, 5183 (2002).
- ⁴⁵ Y. Deng, Y. Kong, Y. Zheng, C. Zhou, D. Xi, P. Chen, S. Gu, B. Shen, R. Zhang, P. Han, R. Jiang, and Y. Shi, *J. Vac. Sci. Technol. A Vacuum, Surfaces, Film.* **23**, 628 (2005).
- ⁴⁶ M. Sardela, *Practical Materials Characterization* (Springer, 2014).
- ⁴⁷ S.M. Ali, F. Bonnier, H. Lambkin, K. Flynn, V. McDonagh, C. Healy, T.C. Lee, F.M. Lyng, and H.J. Byrne, *Anal. Methods* **5**, 2281 (2013).
- ⁴⁸ M. Kuball, *Surf. Interface Anal.* **31**, 987 (2001).
- ⁴⁹ S. Choi, E. Heller, D. Dorsey, R. Vetury, and S. Graham, *J. Appl. Phys.* **113**, 093510 (2013).
- ⁵⁰ J.G. Tischler and J.A. Freitas, *Appl. Phys. Lett.* **85**, 1943 (2004).
- ⁵¹ A. Sarua, M. Kuball, and J.E. Van Nostrand, *Appl. Phys. Lett.* **81**, 1426 (2002).
- ⁵² A.R. Goni, H. Siegle, K. Syassen, C. Thomsen, and J.M. Wagner, **64**, 035205 (2001).
- ⁵³ J.M. Wagner and F. Bechstedt, *Phys. Status Solidi Basic Res.* **234**, 965 (2002).
- ⁵⁴ J. Wang, D. Chen, Y. Xu, Q. Liu, and L. Zhang, *J. Spectrosc.* **2013**, 103602 (2013).
- ⁵⁵ D. Chen, D. Xu, J. Wang, B. Zhao, and Y. Zhang, *Thin Solid Films* **517**, 986 (2008).
- ⁵⁶ J.M. Wagner and F. Bechstedt, *Appl. Phys. Lett.* **77**, 346 (2000).
- ⁵⁷ J. Gleize, M.A. Renucci, J. Frandon, E. Bellet-Amalric, and B. Daudin, *J. Appl. Phys.* **93**, 2065 (2003).
- ⁵⁸ V.Y. Davydov, Y.E. Kitaev, I. Goncharuk, A. Smirnov, J. Graul, O. Semchinova, and D. Uffmann, *Phys. Rev. B - Condens. Matter Mater. Phys.* **58**, 12899 (1998).
- ⁵⁹ Y. Dai, S. Li, Q. Sun, Q. Peng, C. Gui, Y. Zhou, and S. Liu, *J. Cryst. Growth* **435**, 76 (2016).
- ⁶⁰ J.M. Wagner and F. Bechstedt, *Phys. Rev. B - Condens. Matter Mater. Phys.* **66**, 115202 (2002).
- ⁶¹ S. Yang, R. Miyagawa, H. Miyake, K. Hiramatsu, and H. Harima, *Appl. Phys. Express* **4**, 031001 (2011).

- ⁶² W. Zhu, A. Leto, K.Y. Hashimoto, and G. Pezzotti, *J. Appl. Phys.* **112**, 103526 (2012).
- ⁶³ H.J. Trodahl, F. Martin, P. Muralt, and N. Setter, *Appl. Phys. Lett.* **89**, 061905 (2006).
- ⁶⁴ X. Rong, X. Wang, G. Chen, J. Pan, P. Wang, H. Liu, F. Xu, P. Tan, and B. Shen, *Superlattices Microstruct.* **93**, 27 (2016).
- ⁶⁵ D. Zhang, F.M. Liu, and L.G. Cai, *Phys. Status Solidi Appl. Mater. Sci.* **211**, 2394 (2014).
- ⁶⁶ M. Kazan, C. Zgheib, E. Moussaed, and P. Masri, *Diam. Relat. Mater.* **15**, 1169 (2006).
- ⁶⁷ T. Prokofyeva, M. Seon, J. Vanbuskirk, M. Holtz, S.A. Nikishin, N.N. Faleev, H. Temkin, and S. Zollner, *Phys. Rev. B - Condens. Matter Mater. Phys.* **63**, 125313 (2001).
- ⁶⁸ K.R. Bagnall and E.N. Wang, *Rev. Sci. Instrum.* **87**, 061501 (2016).
- ⁶⁹ L. Ben Freund and S. Suresh, *Thin Film Materials: Stress, Defect Formation and Surface Evolution* (Cambridge University Press, 2004).
- ⁷⁰ M. Ohring, *Materials Science of Thin Films* (Elsevier, 2001).
- ⁷¹ S. Figge, H. Kröncke, D. Hommel, and B.M. Epelbaum, *Appl. Phys. Lett.* **94**, 101915 (2009).
- ⁷² B. Yates, R.F. Cooper, and A.F. Pojur, *J. Phys. C Solid State Phys.* **5**, 1046 (1972).
- ⁷³ K. Tsubouchi and N. Mikoshiba, *IEEE Trans. Sonics Ultrason.* **32**, 634 (1985).
- ⁷⁴ J.H. Gieske and G.R. Barsch, *Phys. Status Solidi* **29**, 121 (1968).
- ⁷⁵ R.M. Spriggs, *J. Am. Ceram. Soc.* **44**, 628 (1961).
- ⁷⁶ K. Zeng, F. Zhu, J. Hu, L. Shen, K. Zhang, and H. Gong, *Thin Solid Films* **443**, 60 (2003).
- ⁷⁷ K.R. Bagnall, E.A. Moore, S.C. Badescu, L. Zhang, and E.N. Wang, *Rev. Sci. Instrum.* **88**, 113111 (2017).
- ⁷⁸ P. Giannozzi, S. Baroni, N. Bonini, M. Calandra, R. Car, C. Cavazzoni, D. Ceresoli, G.L. Chiarotti, M. Cococcioni, I. Dabo, A. Dal Corso, S. De Gironcoli, S. Fabris, G. Fratesi, R. Gebauer, U. Gerstmann, C. Gougoussis, A. Kokalj, M. Lazzeri, L. Martin-Samos, N. Marzari, F. Mauri, R. Mazzarello, S. Paolini, A. Pasquarello, L. Paulatto, C. Sbraccia, S. Scandolo, G. Sclauzero, A.P. Seitsonen, A. Smogunov, P. Umari, and R.M. Wentzcovitch, *J. Phys. Condens. Matter* **21**, 395502 (2009).
- ⁷⁹ S. Baroni, S. De Gironcoli, A. Dal Corso, and P. Giannozzi, *Rev. Mod. Phys.* **73**, 515 (2001).
- ⁸⁰ R. Resta, *Rev. Mod. Phys.* **66**, 899 (1994).
- ⁸¹ I. Vurgaftman and J.R. Meyer, *J. Appl. Phys.* **94**, 3675 (2003).
- ⁸² G.A. Slack, *J. Phys. Chem. Solids* **34**, 321 (1973).
- ⁸³ H. Schulz and K.H. Thiemann, *Solid State Commun.* **23**, 815 (1977).
- ⁸⁴ W. Paszkowicz, S. Podsiadło, and R. Minikayev, *J. Alloys Compd.* **382**, 100 (2004).
- ⁸⁵ T. Kozawa, T. Kachi, H. Kano, Y. Taga, M. Hashimoto, N. Koide, and K. Manabe, *J. Appl. Phys.* **75**, 1098 (1994).
- ⁸⁶ C. Kisielowski, J. Krüger, S. Ruvimov, T. Suski, J.W. Ager, E. Jones, Z. Liliental-Weber, M. Rubin, E.R. Weber, M.D. Bremser, and R.F. Davis, *Phys. Rev. B* **54**, 17745 (1996).
- ⁸⁷ M. Kuball and J.W. Pomeroy, *IEEE Trans. Device Mater. Reliab.* **16**, 667 (2016).
- ⁸⁸ O. Kluth, G. Schöpe, B. Rech, R. Menner, M. Oertel, K. Orgassa, and H.W. Schock, *Thin Solid Films* **502**, 311 (2006).
- ⁸⁹ G. Ross, H. Dong, C.B. Karuthedath, A.T. Sebastian, T. Pensala, and M. Paulasto-Kröckel, *Mater. Des.* **196**, 109126 (2020).
- ⁹⁰ S. Mertin, B. Heinz, O. Rattunde, G. Christmann, M.-A. Dubois, S. Nicolay, and P. Muralt, *Surf. Coatings Technol.* **343**, 2 (2018).
- ⁹¹ K. Bespalova, E. Österlund, G. Ross, M. Paulasto-Kröckel, A.T. Sebastian, C.B. Karuthedath, S. Mertin, and T. Pensala, *J. Microelectromechanical Syst.* **30**, 290 (2021).
- ⁹² J. Guo, C. Liu, T. Han, and J. Miao, in *2017 Symp. Piezoelectricity, Acoust. Waves, Device Appl.* (2017), pp. 211–216.
- ⁹³ K. Ait Aissa, A. Achour, J. Camus, L. Le Brizoual, P.Y. Jouan, and M.A. Djouadi, *Thin Solid Films* **550**, 264 (2014).

⁹⁴ K. Kusaka, D. Taniguchi, T. Hanabusa, and K. Tominaga, *Vacuum* **66**, 441 (2002).

⁹⁵ M.-A. Dubois and P. Muralt, *J. Appl. Phys.* **89**, 6389 (2001).

⁹⁶ Y. Qiu, J. V Gigliotti, M. Wallace, F. Griggio, C.E.M. Demore, S. Cochran, and S. Trolier-McKinstry, *Sensors* **15**, 8020 (2015).

Figure Captions

Fig. 1. Raman spectra of an AlN film sputter deposited on Si, an AlN film grown via plasma vapor deposition on sapphire, and a free-standing bulk AlN substrate grown via a combination of physical vapor transport and seeded growth. The E_2 (low), E_2 (high), and A_1 (LO) phonons are highlighted across all Raman spectra. The stars and inverted triangles denote Si and sapphire Raman peaks, respectively.

Fig. 2. The change in frequency $\Delta\omega$ as a function of temperature rise ΔT for bulk and thin film (400 nm) AlN (left axis). The absolute value of the difference between $\Delta\omega$ for bulk and thin film AlN is also shown as a function of ΔT (right axis).

Fig. 3. The dependence of the frequency shifts of the (a) E_2 (low), (b) E_2 (high), and (c) A_1 (LO) phonon modes as a function of stress as determined by the thermomechanical analysis method for Samples 1-3 (Table II). The slope of the linear fit in the equations shown for each sample and phonon mode are the corresponding biaxial stress coefficients.

Fig. 4. Spatial distribution of residual stress (squares, left axis) and film thickness (triangles, right axis) across the diameter of an AlN-on-Si wafer.

Fig. 5. (a) Cross-sectional schematic of the AlN pMUTs. (b) Top-view schematic diagram of the pMUT and stress map. Regions A, B, and C are defined. (c) Residual stress distribution as a function of measurement number. The schematic in (a) is not drawn to scale.

Fig. 6. (a) Measured frequency response of five different pMUTs. The inset of (a) shows the location of reticles 4-8 on the AlN/Si wafer. (b) The first, second, and third order resonant frequencies are compared with the measured residual stresses in the five pMUTs.

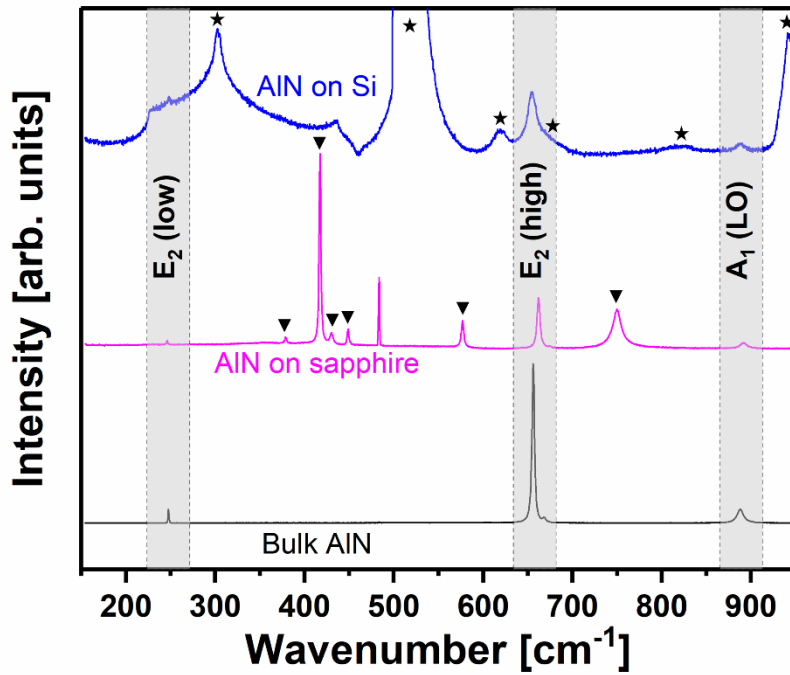


Fig. 1. Raman spectra of an AlN film sputter deposited on Si, an AlN film grown via plasma vapor deposition on sapphire, and a free-standing bulk AlN substrate grown via a combination of physical vapor transport and seeded growth. The E₂ (low), E₂ (high), and A₁ (LO) phonons are highlighted across all Raman spectra. The stars and inverted triangles denote Si and sapphire Raman peaks, respectively.

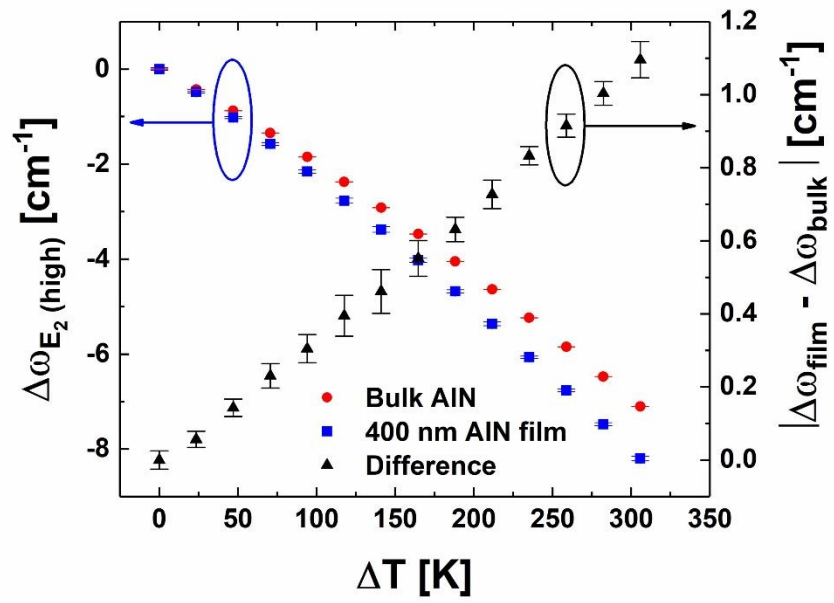


Fig. 2. The change in frequency $\Delta\omega$ as a function of temperature rise ΔT for bulk and thin film (400 nm) AlN (left axis). The absolute value of the difference between $\Delta\omega$ for bulk and thin film AlN is also shown as a function of ΔT (right axis).

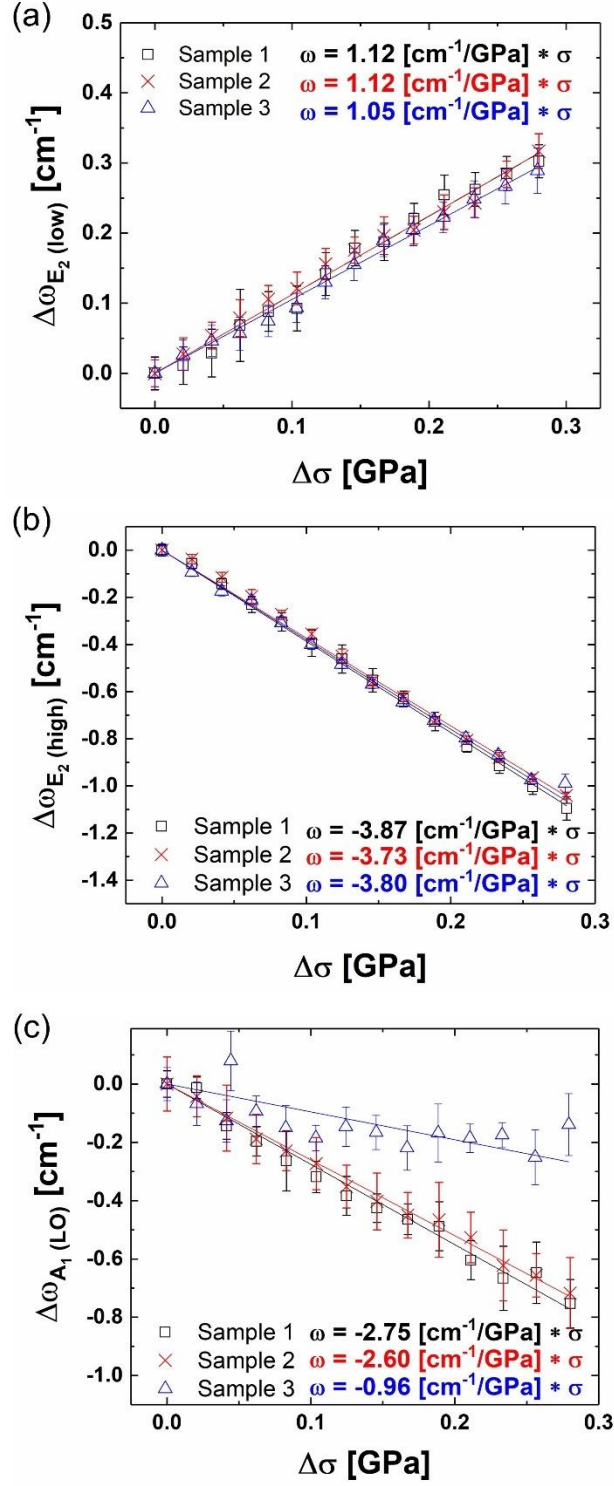


Fig. 3. The dependence of the frequency shifts of the (a) E_2 (low), (b) E_2 (high), and (c) A_1 (LO) phonon modes as a function of stress as determined by the thermomechanical analysis method for Samples 1-3 (Table II). The slope of the linear fit in the equations shown for each sample and phonon mode are the corresponding biaxial stress coefficients.

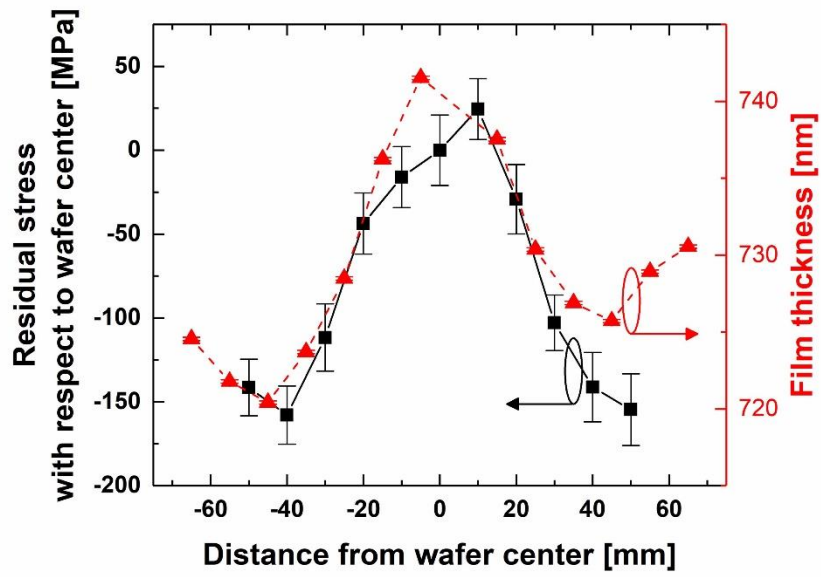


Fig. 4. Spatial distribution of residual stress (squares, left axis) and film thickness (triangles, right axis) across the diameter of an AlN-on-Si wafer.

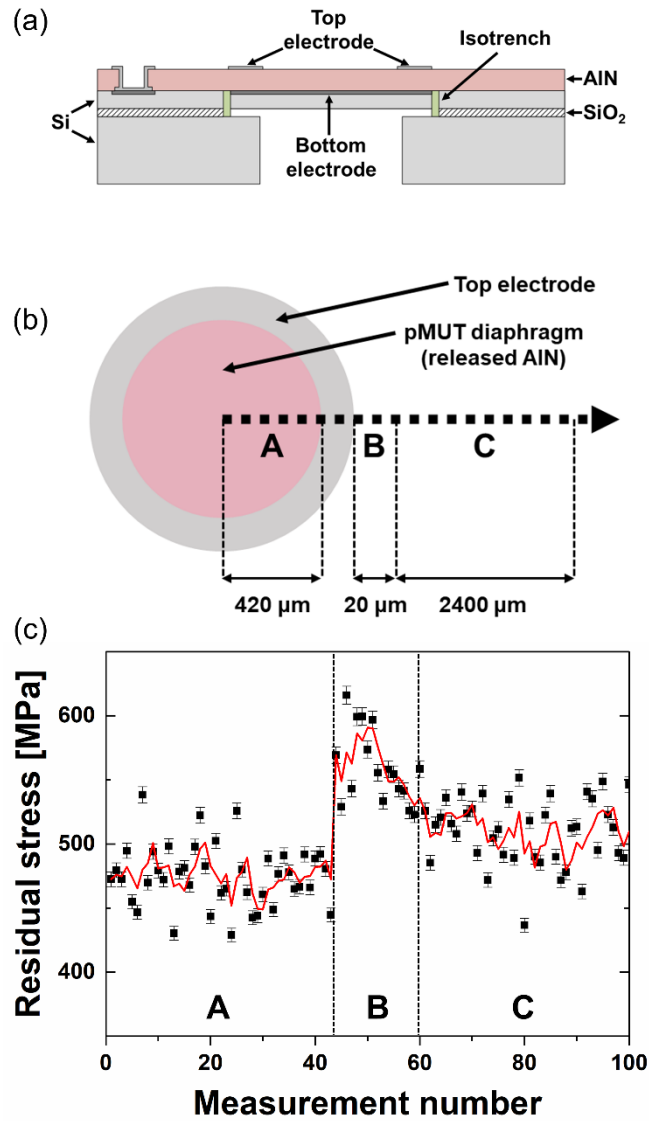


Fig. 5. (a) Cross-sectional schematic of the AlN pMUTs. (b) Top-view schematic diagram of the pMUT and stress map. Regions A, B, and C are defined. (c) Residual stress distribution as a function of measurement number. The solid line is a three-point moving average. The schematic in (a) is not drawn to scale.

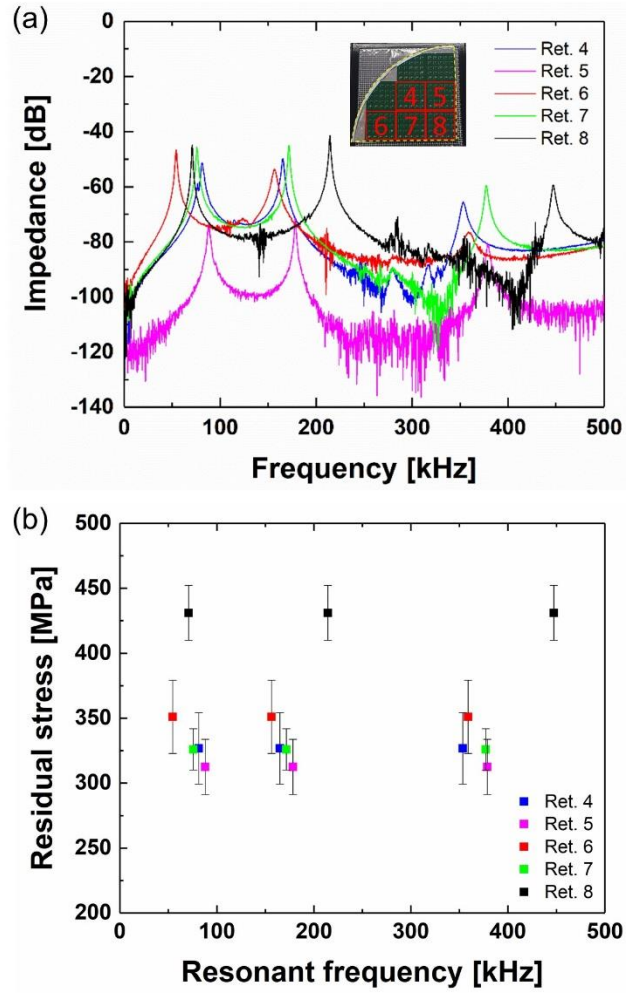


Fig. 6. (a) Measured frequency response of five different pMUTs. The inset of (a) shows the location of reticles 4-8 on the AlN/Si wafer. (b) The first, second, and third order resonant frequencies are compared with the measured residual stresses in the five pMUTs.

Tables

Table I. Previously reported values of the strain-free frequencies ω_0 and biaxial stress coefficients K^{II} for the E₂ (low), E₂ (high), and A₁ (LO) phonon modes of wurtzite aluminum nitride.

Ref.	E ₂ (low) ω_0 [cm ⁻¹]	E ₂ (high) ω_0 [cm ⁻¹]	A ₁ (LO) ω_0 [cm ⁻¹]	E ₂ (low) K^{II} [cm ⁻¹ /GPa]	E ₂ (high) K^{II} [cm ⁻¹ /GPa]	A ₁ (LO) K^{II} [cm ⁻¹ /GPa]
1	252	660	893			
13					-4.7 ± 0.5	
15		654			-3.5 ± 0.5	
27		658			-3.7 ± 0.3	
50	246.1 ± 0.5	655.1 ± 0.5	888.9 ± 0.5			
51					-3 ± 0.4	
52	247.5 ± 0.5	655.5 ± 0.1	891			
53					-2.55	
54		657.1			-4.45	
55		657.6			-4.1 ± 0.3	
56				0.94	-2.56	-2.22
57					-3.39 ± 0.64	-1.39 ± 0.28
58	248.6 ± 0.2	657.4 ± 0.2	890 ± 0.2			
59	247.3	656.52		0.713	-4.423	
60	241	667	898	0.94	-2.55	-2.21
61		657.67			-4.04 ± 0.3	
62					-3.4 ± 0.22	-3.12 ± 0.58
63		656			-2.9 ± 0.3	
64		657.8 ± 0.3			-2.4 ± 0.2	
65					-1.9	
66	247.8	656.5	888.4			
67		657.4 ± 0.2			-6.3 ± 1.4	

Table II. Details of the 4 AlN samples used in the thermomechanical analysis approach.

Sample Number	Substrate	AlN thickness [nm]	Deposition/Growth Method
1	Sapphire	400	PVDNC*
2	Sapphire	481	PVT
3	Sapphire	1007	HVPE
4	AlN (bulk)	6×10^5 (bulk)	Seeded/PVT

*Plasma vapor deposition with nanocolumns

Table III. Summary of the biaxial stress coefficients of the E₂ (low), E₂ (high), and A₁ (LO) phonon modes of wurtzite AlN determined in this study. The two submethods listed in “DFT” are two adaptations of the DFT modeling approach.

Method	Submethod	E₂ (low) K'' [cm⁻¹/GPa]	E₂ (high) K'' [cm⁻¹/GPa]	A₁ (LO) K'' [cm⁻¹/GPa]
Thermomechanical analysis	N/A	1.10 ± 0.02	-3.80 ± 0.04	-2.68 ± 0.04
	PBESol	0.77	-3.46	-2.08
DFT	PZ	0.82	-3.46	-2.36

Table IV. Recommended values of the strain-free phonon frequencies and biaxial stress coefficients for the E₂ (low), E₂ (high), and A₁ (LO) phonon modes of wurtzite AlN.

	ω_0 [cm ⁻¹]	K'' [cm ⁻¹ /GPa]
E₂ (low)	247.84 ± 0.004	1.10 ± 0.02
E₂ (high)	656.68 ± 0.003	-3.80 ± 0.04
A₁ (LO)	888.97 ± 0.005	-2.68 ± 0.04

Residual stress analysis of aluminum nitride piezoelectric micromachined ultrasonic transducers using Raman spectroscopy

James Spencer Lundh¹, Kathleen Coleman², Yiwen Song¹, Benjamin A. Griffin³, Giovanni Esteves³, Erica A. Douglas³, Adam Edstrand³, Stefan C. Badescu⁴, Elizabeth A. Moore⁴, Jacob H. Leach⁵, Baxter Moody⁶, Susan Trolrier-McKinstry², and Sukwon Choi^{1,a)}

¹ Department of Mechanical Engineering, The Pennsylvania State University, University Park, PA, 16802, USA

² Department of Materials Science and Engineering, The Pennsylvania State University, University Park, PA, 16802, USA

³ Sandia National Laboratories, Albuquerque, NM, 87185, USA

⁴ Air Force Research Laboratory, Wright-Patterson Air Force Base, OH, 45433, USA

⁵ Kyma Technologies, Inc., Raleigh, NC, 27617, USA

⁶ HexaTech, Inc., Morrisville, NC, 27560, USA

^{a)} Author to whom correspondence should be addressed: sukwon.choi@psu.edu

Strain and stress phonon deformation potentials (PDPs)

Phonon deformation potential theory describes the change in the interatomic potential of the crystal due to small perturbations arising from strain. The change in the interatomic potential results in a shift of phonon frequency. For wurtzite AlN, belonging to the C_{6v} point group, the shifts in phonon frequency $\Delta\omega$ for the zone-center E_2 and A_1 optical phonons as a function of strain ϵ are given in Cartesian coordinates by ¹:

$$\Delta\omega_{E_2} = a_{E_2}(\epsilon_{xx} + \epsilon_{yy}) + b_{E_2}\epsilon_{zz} \pm c_{E_2} \left[(\epsilon_{xx} - \epsilon_{yy})^2 + 4\epsilon_{xy}^2 \right]^{1/2} \quad (\text{S.1a})$$

$$\Delta\omega_{A_1} = a_{A_1}(\epsilon_{xx} + \epsilon_{yy}) + b_{A_1}\epsilon_{zz} \quad (\text{S.1b})$$

where a,b, and c are the strain phonon deformation potentials (PDPs). The strain, ϵ_i , induced in the crystal lattice can be described according to the constitutive equation below in Voigt notation:

$$\epsilon_i = s_{ij}\sigma_j + \alpha_i\Delta T + d_{ki}E_k \quad (\text{S.2})$$

$(i, j = 1, 2, \dots, 6 ; k = 1, 2, 3).$

In this equation, s_{ij} is the compliance coefficient matrix, σ_j is the stress tensor, α_i is the thermal expansion coefficient vector, ΔT is the temperature change, d_{ki} is the piezoelectric coefficient matrix, and E_k is the electric field vector. For the case of residual stress in thin films, there is no

contribution to strain from temperature induced thermal expansion ($\alpha_i \Delta T = 0$) or electric field induced piezoelectricity ($d_{ki} E_k = 0$); therefore, Supplementary Equation (S.2) can be simplified to:

$$\epsilon_i = s_{ij} \sigma_j \quad (S.3)$$

$$(i, j = 1, 2, \dots, 6)$$

For all classes of the hexagonal crystal system, the compliance matrix is given by ²:

$$(s_{ij}) = \begin{bmatrix} s_{11} & s_{12} & s_{13} & 0 & 0 & 0 \\ s_{12} & s_{11} & s_{13} & 0 & 0 & 0 \\ s_{13} & s_{13} & s_{33} & 0 & 0 & 0 \\ 0 & 0 & 0 & s_{44} & 0 & 0 \\ 0 & 0 & 0 & 0 & s_{44} & 0 \\ 0 & 0 & 0 & 0 & 0 & 2(s_{11} - s_{12}) \end{bmatrix} \quad (S.4)$$

Combining Supplementary Equations (S.3) and (S.4) and inserting into Supplementary Equations (S.1a) and (S.1b), the shifts in phonon frequency as a function of stress are obtained for the E₂ and A₁ phonons:

$$\begin{aligned} \Delta\omega_{E_2} = & [a_{E_2}(s_{11} + s_{12}) + b_{E_2}s_{13}](\sigma_{xx} + \sigma_{yy}) \\ & + (2a_{E_2}s_{13} + b_{E_2}s_{33})\sigma_{zz} \\ & \pm c_{E_2}|s_{11} - s_{12}| \left[(\sigma_{xx} - \sigma_{yy})^2 + 16\sigma_{xy}^2 \right]^{1/2} \end{aligned} \quad (S.5a)$$

$$\begin{aligned} \Delta\omega_{A_1} = & [a_{A_1}(s_{11} + s_{12}) + b_{A_1}s_{13}](\sigma_{xx} + \sigma_{yy}) \\ & + (2a_{A_1}s_{13} + b_{A_1}s_{33})\sigma_{zz} \end{aligned} \quad (S.5b)$$

The state of residual stress in thin films is assumed to be biaxial in the in-plane directions ($\sigma_{xx} = \sigma_{yy}$, $\sigma_{xx} \cong 0$) with negligible shear stress in the xy-plane ($\sigma_{xy} \cong 0$). These assumptions simplify Supplementary Equations (S.5a) and (S.5b) such that the relations between phonon frequency shift and biaxial stress are the same for the E₂ and A₁ phonons with the exception of phonon-independent strain PDPs, a_n and b_n :

$$\Delta\omega_n = 2[a_n(s_{11} + s_{12}) + b_n s_{13}] \sigma_{xx} \quad (S.6)$$

Using the following relations between the compliance and stiffness coefficients:

$$s_{11} + s_{12} = \frac{c_{33}}{c_{33}(c_{11} + c_{12}) - 2c_{13}^2} \quad (S.7a)$$

$$s_{13} = -\frac{c_{13}}{c_{33}(c_{11} + c_{12}) - 2c_{13}^2}, \quad (S.7b)$$

it is possible to present the phonon frequency shift due to biaxial stress through the introduction of a stress PDP, \tilde{a}_n :

$$\Delta\omega_n = 2\tilde{a}_n\sigma_{xx} \quad (\text{S.8a})$$

where

$$\tilde{a}_n = \frac{a_n C_{33} - b_n C_{13}}{C_{33}(C_{11} + C_{12}) - 2C_{13}^2} \quad (\text{S.8b})$$

Using the notation of Ref. ³, the final equation describing the relation between phonon frequency shift and biaxial stress in the c-plane is given by:

$$\Delta\omega_n = K_n^{II} \sigma_{xx} \quad (\text{S.9})$$

where K_n^{II} [cm⁻¹/GPa] is the biaxial stress coefficient for the n phonon mode. From Supplementary Equations (S.6) – (S.9), it can be seen that the biaxial stress coefficients for the AlN phonon modes depend on the strain PDPs a_n and b_n and the stiffness coefficients of AlN.

Comparison of the COMSOL Multiphysics model with a simple analytical solution

The thermomechanical analysis approach utilizes temperature-induced thermoelastic stresses to determine the biaxial stress coefficients. For free-standing bulk AlN, it is assumed that isothermal heating results in stress-free thermal expansion. Therefore, the frequency shift $\Delta\omega_{bulk}$ of the E_2 (low), E_2 (high), and A_1 (LO) phonons in free-standing bulk AlN should be solely due to temperature-induced volumetric expansion $\Delta\omega_V$ and phonon decay processes $\Delta\omega_D$ as a result of the anharmonicity of the lattice potential ⁴:

$$\Delta\omega_{bulk} = \Delta\omega_V + \Delta\omega_D \quad (\text{S.10})$$

For an AlN thin film on a foreign substrate, thermoelastic stresses are induced by isothermal heating of the heterostructure due to the mismatch in the coefficients of thermal expansion between the AlN film and the substrate. These thermoelastic stresses introduce an additional contribution $\Delta\omega_S$ to the frequency shift $\Delta\omega_{film}$ of the phonons in the thin film AlN:

$$\Delta\omega_{film} = \Delta\omega_V + \Delta\omega_D + \Delta\omega_S \quad (\text{S.11})$$

Accordingly, the temperature dependence of the phonon frequency shifts in free-standing bulk AlN and thin film AlN will be different. This difference should be a result of thermally-induced biaxial stresses in the film given by subtracting Supplementary Equation (S.10) from Supplementary Equation (S.11):

$$\Delta\omega_{film} - \Delta\omega_{bulk} = \Delta\omega_S \quad (\text{S.12})$$

In Figure 2, the difference between the frequency shift of the E_2 (high) phonon mode for free-standing bulk AlN and a 400 nm AlN thin film is shown (Table II, Sample 1). As shown, this difference follows an approximately linear relationship which is related to the E_2 (high) biaxial stress coefficient K^{II} and thermoelastic biaxial stress $\Delta\sigma$ by:

$$\Delta\omega_S = K_{E_2 (high)}^{II} \Delta\sigma \quad (\text{S.13})$$

The temperature dependence of the thermoelastic biaxial stress induced in the thin film can be computed by varying the environmental temperature in a thermomechanical model of the heterostructure using COMSOL Multiphysics. Therefore, the biaxial stress coefficients for the phonon modes of AlN can be determined using this modeled stress and the measured frequency shifts. In this study, the temperature dependence of the phonons in three AlN/sapphire heterostructures and a free-standing bulk AlN substrate (Table II) were measured using Raman spectroscopy. It should be noted that although the AlN film of Sample 1 from Table II was deposited via nanocolumnar growth (plasma vapor deposition with nanocolumns; PVDNC), the nanocolumns are very dense and no voids are observed when using atomic force microscopy (AFM) and transmission electron microscopy (TEM), as shown in Supplementary Figure 1. AFM topography is also shown for Samples 2 and 3 from Table II. In order to determine these

thermoelastic stresses, a 3D thermomechanical model of three AlN/sapphire heterostructures (Table II, Samples 1-3) was constructed. Temperature dependent coefficients of thermal expansion (CTEs) were used for both AlN and sapphire in the model. These temperature dependent CTEs are given in Supplementary Table I for AlN⁵ and sapphire⁶. The stiffness coefficients for thin film AlN reported in⁷ and for sapphire in⁸ were used. Since the experimental method assumes a state of biaxial stress when measuring the in-plane residual stress, it was important to confirm that the stress state of the modeled film was also biaxial in nature. As shown in Supplementary Figure 2, the modeled stresses in the c-plane (σ_{xx} , σ_{yy}) are approximately identical while the shear stress (σ_{xy}) and out-of-plane stress (σ_{zz}) are negligible, validating the assumption of biaxial stress in the c-plane in the model.

The temperature dependence of the thermoelastic biaxial stress induced in the thin film can also be computed using the following simple analytical model for thermal stress of a film on a substrate⁹:

$$\Delta\sigma(T) = \int_{T_1}^{T_2} B_f (\alpha_s - \alpha_f) dT \quad (\text{S.14})$$

where B_f is the biaxial modulus of the film and α_s and α_f are the coefficients of thermal expansion for the substrate and film, respectively. In Supplementary Equation (S.14), B_f is defined by both the elastic modulus E_f and Poisson's ratio ν_f of the wurtzite AlN film as⁹:

$$B_f = \frac{E_f}{1-\nu_f} \quad (\text{S.15a})$$

$$E_f = \frac{c_{11}^2 c_{33} - 2c_{13}^2 c_{11} - c_{12}^2 c_{33} + 2c_{13}^2 c_{12}}{c_{11} c_{33} - c_{13}^2} \quad (\text{S.15b})$$

$$\nu_f = \frac{c_{12} c_{33} - c_{13}^2}{c_{11} c_{33} - c_{13}^2} \quad (\text{S.15c})$$

In Supplementary Figure 3, the stress calculated using the simple analytical equation in Supplementary Equations (S.14) and (S.15) was compared to those computed from the COMSOL Multiphysics model. These modeled stresses are plotted in Supplementary Figure 3 and they show very good agreement.

Validation of the biaxial stress coefficients and strain-free phonon frequencies

After determining the biaxial stress coefficients and strain-free phonon frequencies, a validation study was performed. This was accomplished by measuring the frequencies of the E_2 (low), E_2 (high), and A_1 (LO) phonons of several AlN thin films using Raman spectroscopy. Subsequently, ω_0 and K^{II} determined in Section 3.1 were applied to compare the residual stress calculated using all three phonon modes in the various films.

The validation study was performed on 13 AlN thin films (Supplementary Table 2). This includes AlN films of various thicknesses (45-750 nm), different substrates (sapphire and Si), and grown through different methods (plasma vapor deposition and reactive pulsed-DC magnetron sputtering). The PVDNC films (Supplementary Table II, Samples 1-4) were grown using Kyma's modified AlN sputtering technique to produce nanocolumnar arrays of AlN structures. The AlN films of Samples 5-13 in Supplementary Table II were deposited via reactive sputter deposition on 150 mm n-type Si (100) wafers using an SPTS Sigma 200 pulsed DC magnetron deposition tool. For each deposition, 5 kW of target power, a platen temperature of 350 °C, and an Ar/N₂ flow rate of 20/100 sccm were used. Films targeted a thickness of 750 nm and the average film stress was varied by changing the RF substrate bias power from 0 W to 150 W. Accordingly, the average residual stress in these films was measured to range from -1708 MPa (compressive) to 784 MPa (tensile) based on wafer curvature measurements. SEM top-side imaging of Samples 9 and 10 is also shown in Supplementary Figures 1(e) and 1(f).

As shown in Supplementary Figure 4(a), there is good qualitative agreement in the measured residual stress among all three phonon modes. However, for some samples, there is some quantitative inconsistency amongst the three phonon modes when attempting to measure the residual stress in the validation study. For example, the residual stresses measured for Sample 5 vary from ~150 MPa to ~600 MPa.

One possible explanation for this inconsistency could be that the stress state of the films is not truly biaxial in nature. This would not be consistent with the assumption that there is biaxial stress in the c-plane of the film which is required for the derivation and quantitative use of the biaxial stress coefficient K^{II} . To investigate this possibility, XRD was performed on all 13 AlN samples in Supplementary Table II. AlN films were characterized through XRD on a PANalytical X'Pert³ MRD diffractometer. The beam was first aligned in the ω and Z, and then each film was scanned in the 2θ around the (002) and (004) peaks (from 30-40° and 70-80°, respectively). Afterwards, the rocking curve on the (002) peak was obtained to determine the films crystalline quality. To determine the a lattice constant, the off-axis peak (101) from a 2θ - ω scan was used. Pearson VII fitting for the peaks was used to determine the Full Width Half Maxima (FWHM) and the exact θ values to calculate the interplanar separation distance (d) using Bragg's law (**Equation S.16**). The relationship between a hexagonal crystal structure's lattice constants (a and c) and d are shown in **Equation S.17**.

$$2d\sin\theta = n\lambda \quad (\text{S.16})$$

$$d_{hkl} = \left[\left(\frac{4}{3a^2} \right) (h^2 + k^2 + hk) + \left(\frac{l^2}{c^2} \right) \right]^{-1/2} \quad (\text{S.17})$$

where h , k , and l are peak indices for the respective crystallographic planes. The free-standing bulk AlN sample (Table II, Sample 4) was also measured to use as a strain-free reference sample. Using XRD, the unstrained lattice parameters a_0 and c_0 were measured to be 3.11 Å and 4.979 Å, respectively.

Using these unstrained lattice parameters, the in-plane (ϵ_a) and out-of-plane (ϵ_c) strains in the films can be determined by:

$$\epsilon_a = \frac{a-a_0}{a_0} \quad (\text{S.18a})$$

$$\epsilon_c = \frac{c-c_0}{c_0} \quad (\text{S.18b})$$

The strain ratio ϵ_c/ϵ_a can then be determined and compared with the theoretical value for biaxial strain in wurtzite AlN given by ¹⁰:

$$\frac{\epsilon_c}{\epsilon_a} = -\frac{2C_{13}}{C_{33}} \quad (\text{S.19})$$

Using the stiffness coefficients reported by Tsubouchi and Mikoshiba ⁷, the strain ratio should be -0.608 for biaxial strain. The strain ratios calculated for the samples in Supplementary Table II are shown in Supplementary Figure 4(b) along with the theoretical value for biaxial strain. As shown in Supplementary Figure 4(b), the strain ratio varies greatly amongst the samples in the validation study. Therefore, the quantitative assessment of residual stress in Supplementary Figure 4(a) could have been compromised due to violation of the assumption of biaxial stress. However, as can be seen in Supplementary Figure 4(b), Sample 1 has a strain ratio of -0.71 which is close to the theoretical value of -0.608. Sample 1 also shows the best agreement for the residual stress calculated using all three phonon modes. These residual stresses are -2.72 ± 0.067 , -2.74 ± 0.032 , and -2.66 ± 0.047 GPa which agree within 3%. Therefore, when the strain state of the film approaches a truly biaxial strain state, the K'' and ω_0 values determined in this study (Table IV) provide consistent, quantitative residual stress measurement capabilities.

Other possible reasons for some quantitative inconsistency amongst the three phonon modes when attempting to measure the residual stress could be phonon-plasmon coupling of the A₁ (LO) mode ¹¹ and very low signal intensity of the E₂ (low) and A₁ (LO) modes. The A₁ (LO) mode is also very sensitive to free carrier concentration which will shift the phonon frequency separately from residual stress. Moreover, as shown in Figure 1, the intensities of the E₂ (low) and A₁ (LO) modes are very low with respect to the E₂ (high) mode. Low intensity and signal-to-noise ratio makes reliable peak processing difficult and it is undesirable. Therefore, when using Raman spectroscopy for residual stress analysis of AlN thin films and devices, it is recommended that the E₂ (high) phonon mode be used. In addition, the E₂ (high) mode is observed to have the greatest sensitivity to stress which also facilitates greater accuracy and confidence in residual stress measurements.

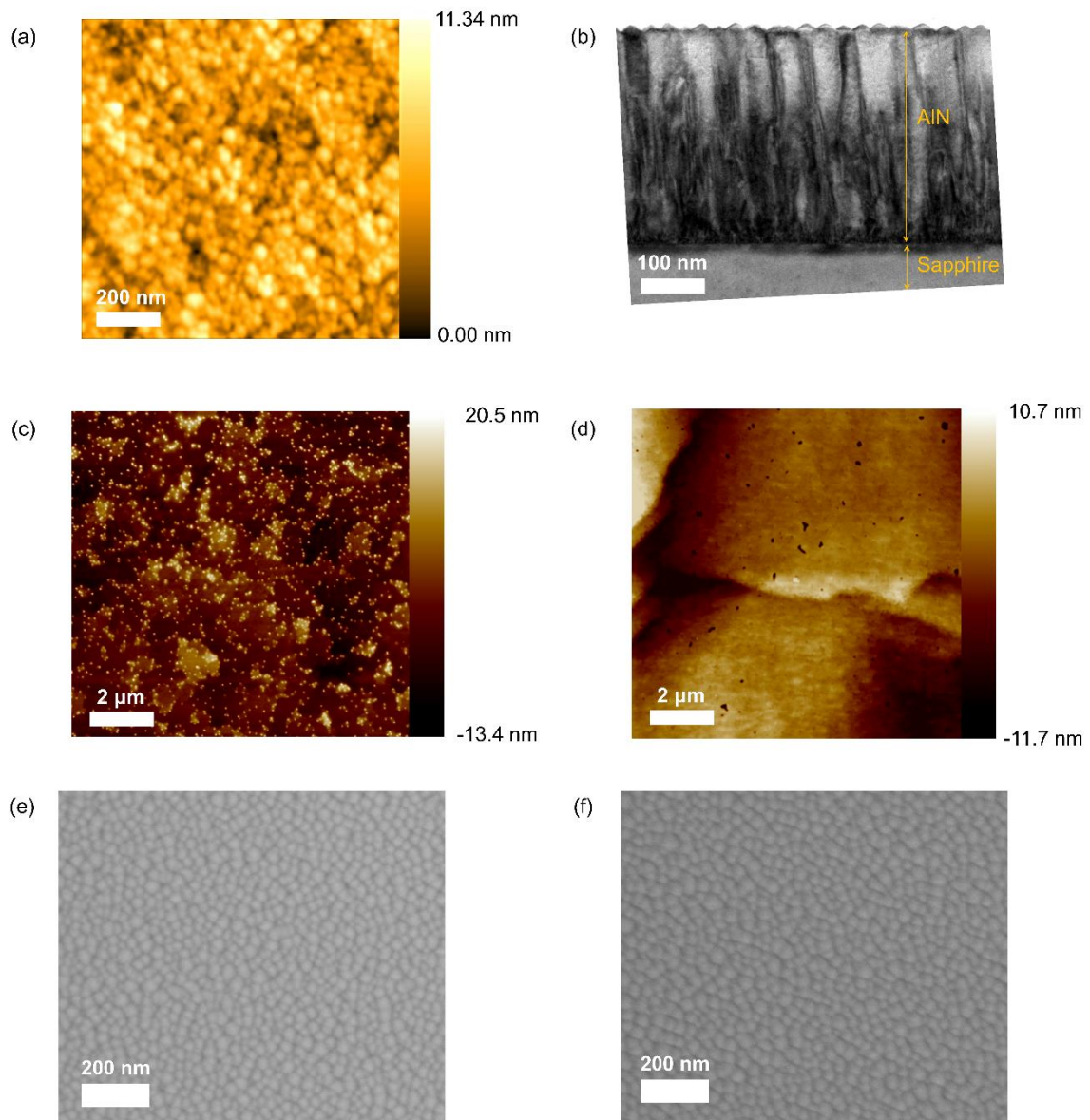
Stress mapping across wafers of varying states of residual stress

Raman spectroscopy was performed on three AlN-on-Si wafers to investigate the residual stress distribution across the wafer at the macroscopic level. To compare the effects of different states of residual stress, stress mapping was performed on wafers with tensile (638 MPa), compressive (-672 MPa), and no residual stress (0 MPa). The average stress states of the wafers were measured using the wafer curvature method. Since the probing depth of the 532 nm laser ($NA = 0.8$) is ≥ 1 μm in materials whose bandgap is greater than the laser energy of ~ 2.33 eV, the entire through thickness of the AlN films (~ 750 nm) was probed. Therefore, a through-thickness average residual stress was measured in the AlN films.

As shown in Supplementary Figure 5(a), the residual stress was found to become more compressive as the distance from the center of the wafer increased. Moreover, the Raman peak intensities of the E_2 (high) phonon decreased with increasing distance from the center of the wafer. These observations were found to scale with the spatial variation in AlN film thickness measured by spectroscopic ellipsometry, as seen in Supplementary Figure 5(b). This correlation was observed for all films regardless of their average state of residual stress. For all films, the difference in thickness from the center of the wafer to ± 5 cm was approximately 20-25 nm. Accordingly, at ± 5 cm, the residual stress in all films was ~ 150 MPa more compressive than at the center of the wafer.

References

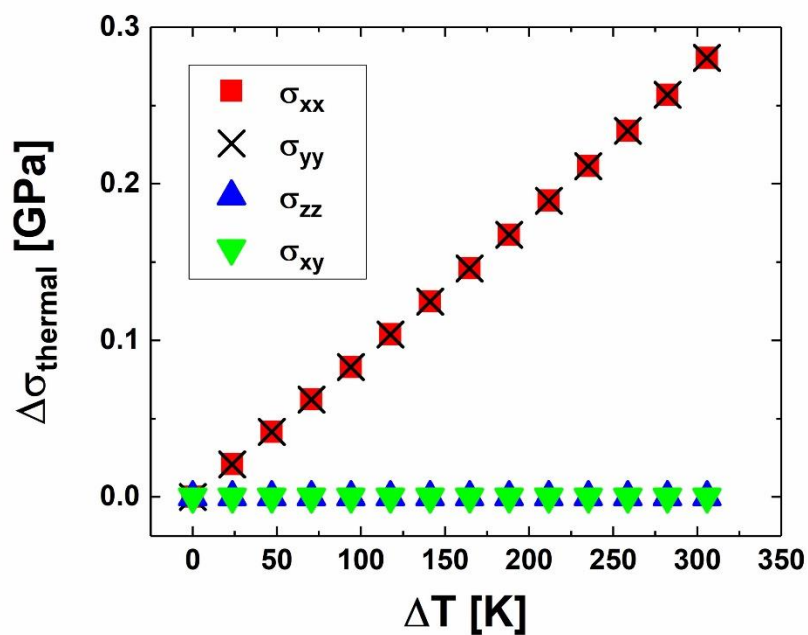
- ¹ R.J. Briggs and A.K. Ramdas, Phys. Rev. B **13**, 5518 (1976).
- ² J.F. Nye, *Physical Properties of Crystals : Their Representation by Tensors and Matrices* (Clarendon, Oxford, 1957).
- ³ K.R. Bagnall and E.N. Wang, Rev. Sci. Instrum. **87**, 061501 (2016).
- ⁴ G. Lucazeau, J. Raman Spectrosc. **34**, 478 (2003).
- ⁵ S. Figge, H. Kröncke, D. Hommel, and B.M. Epelbaum, Appl. Phys. Lett. **94**, 101915 (2009).
- ⁶ B. Yates, R.F. Cooper, and A.F. Pojur, J. Phys. C Solid State Phys. **5**, 1046 (1972).
- ⁷ K. Tsubouchi and N. Mikoshiba, IEEE Trans. Sonics Ultrason. **32**, 634 (1985).
- ⁸ J.H. Gieske and G.R. Barsch, Phys. Status Solidi **29**, 121 (1968).
- ⁹ Y. Dai, S. Li, H. Gao, W. Wang, Q. Sun, Q. Peng, C. Gui, Z. Qian, and S. Liu, J. Mater. Sci. Mater. Electron. **27**, 2004 (2016).
- ¹⁰ C. Kisielowski, J. Krüger, S. Ruvimov, T. Suski, J.W. Ager, E. Jones, Z. Liliental-Weber, M. Rubin, E.R. Weber, M.D. Bremser, and R.F. Davis, Phys. Rev. B **54**, 17745 (1996).
- ¹¹ M. Kuball, Surf. Interface Anal. **31**, 987 (2001).



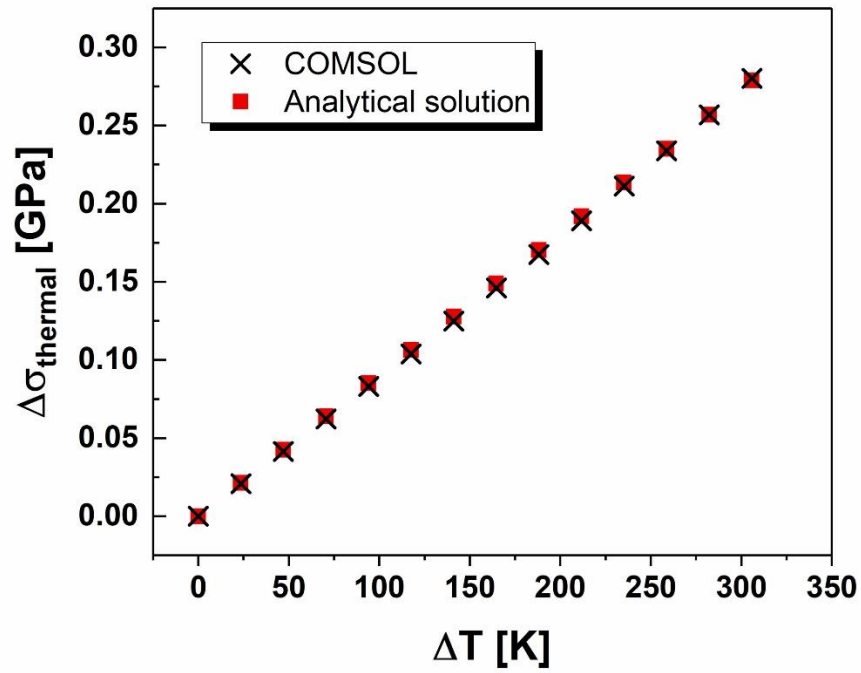
Supplementary Figure 1. (a) AFM topography and (b) TEM cross-sectional imaging of the AlN film of Sample 1 in Table II. AFM topography of the AlN films for (c) Sample 2 and (d) Sample 3 in Table II. Top-side SEM imaging of (e) Sample 9 and (f) Sample 10 in Supplementary Table II.

Supplementary Table I. Temperature dependent coefficient of thermal expansion for aluminum nitride and sapphire used in the 3D thermomechanical model.

Material	Coefficient of thermal expansion α [$\times 10^{-6}$ K$^{-1}$]
Aluminum nitride ₅	$\alpha_a = -2.75$ $+ 2.35 \times 10^{-2}T - 1.65 \times 10^{-5}T^2$
	$\alpha_c = -1.88$ $+ 1.91 \times 10^{-2}T - 1.38 \times 10^{-5}T^2$
Sapphire ₆	$\alpha_a = -0.231$ $+ 2.22 \times 10^{-2}T - 1.48 \times 10^{-5}T^2$
	$\alpha_c = -0.459$ $+ 2.63 \times 10^{-2}T - 1.9 \times 10^{-5}T^2$



Supplementary Figure 2. The change in thermoelastic stress $\Delta\sigma_{thermal}$ as a function of temperature rise ΔT for the 400 nm AlN film (Table II, Sample 1) as determined by the 3D thermomechanical model. σ_{xx} and σ_{yy} are the normal stresses in the c-plane, σ_{zz} is the normal stress in the c-direction, and σ_{xy} is the shear stress in the c-plane.

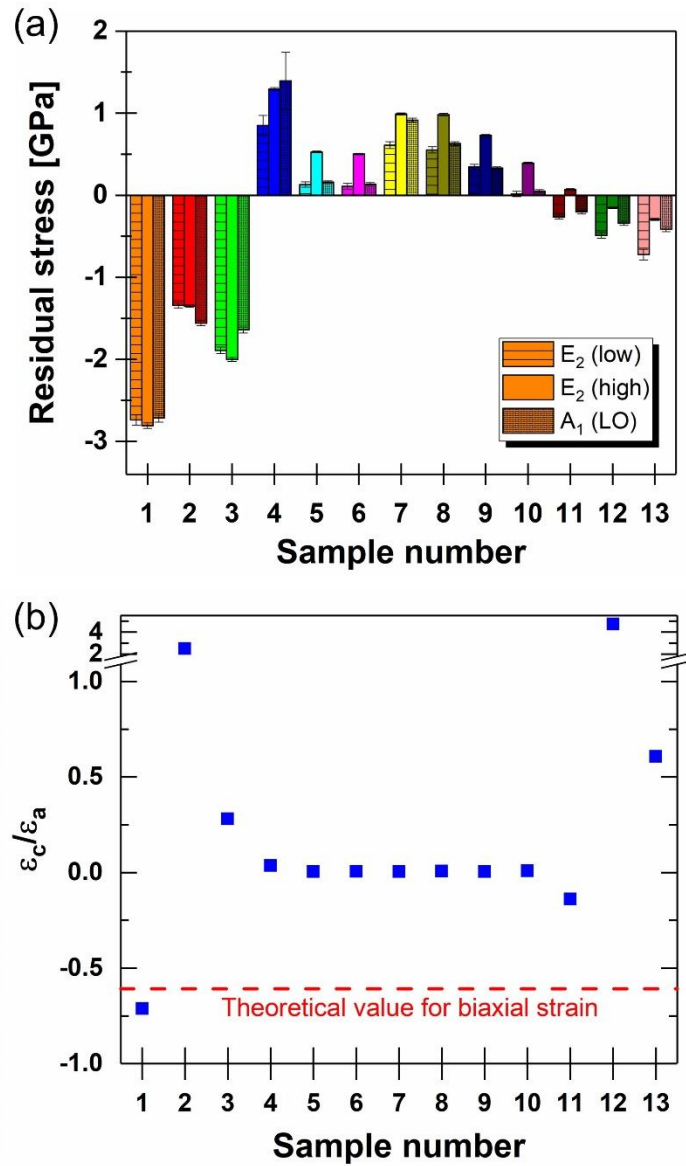


Supplementary Figure 3. The change in thermoelastic stress $\Delta\sigma_{\text{thermal}}$ as a function of temperature rise ΔT determined via the 3D thermomechanical model (crosses) and analytically (squares) using Supplementary Equation S.14.

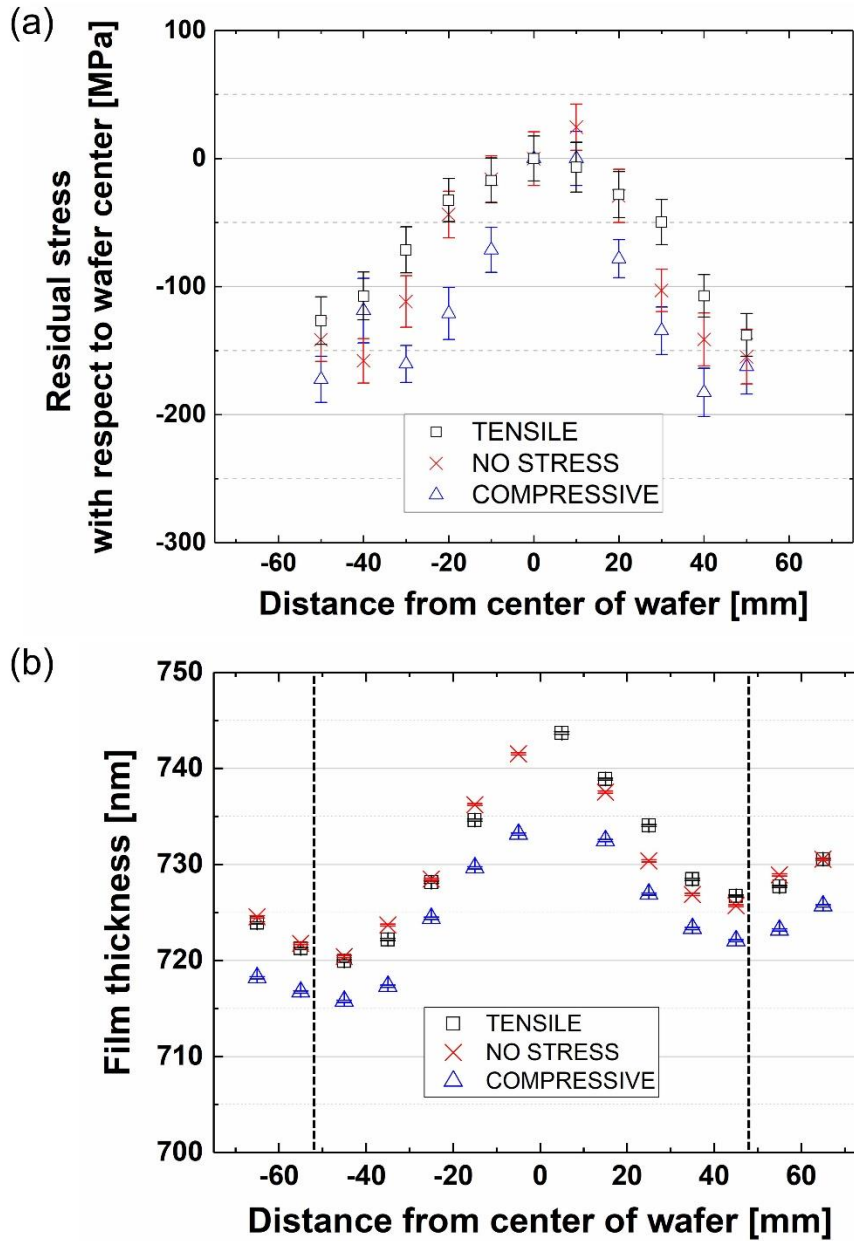
Supplementary Table II. Details of the 13 AlN samples used in the validation study.

Sample Number	Substrate	AlN thickness [nm]	Deposition/ Growth Method	RF Bias [W]
1	Sapphire	45	PVDNC*	N/A
2	Sapphire	215	PVDNC*	N/A
3	Sapphire	350	PVDNC*	N/A
4	Si	200	PVDNC*	N/A
5	Si	750	Sputtered	66
6	Si	750	Sputtered	66
7	Si	750	Sputtered	0
8	Si	750	Sputtered	25
9	Si	750	Sputtered	50
10	Si	750	Sputtered	75
11	Si	750	Sputtered	100
12	Si	750	Sputtered	125
13	Si	750	Sputtered	150

*Plasma vapor deposition with nanocolumns



Supplementary Figure 4. (a) Comparison of the residual stress determined in the 13 AlN films (Supplementary Table II) based on the the E₂ (low), E₂ (high), and A₁ (LO) phonon modes of AlN. (b) The strain ratio ϵ_c/ϵ_a for the samples from (a) calculated using XRD. The red dashed line indicates the theoretical value (-0.608) for biaxial strain in wurtzite AlN.



Supplementary Figure 5. (a) Residual stress distribution across AlN-on-Si wafers with tensile (square), compressive (triangle), and no average residual stress (cross). The residual stress is plotted with respect to the residual stress at the center of the wafer. (b) Thickness of the AlN film across the tensile, compressive, and no average residual stress AlN-on-Si wafers. The vertical dashed lines indicate the extent of the residual stress mapping performed in (a).